Euro. Jnl of Applied Mathematics (2020), *vol.* 31, *pp.* 646–681 © Cambridge University Press 2019.
doi:10.1017/S0956792519000214

Potential flow over a submerged rectangular obstacle: Consequences for initiation of boulder motion

J. G. HERTERICH[1,3] and F. DIAS[1,2,3]

[1]*School of Mathematics and Statistics, University College Dublin, Belfield, Dublin 4, Ireland*
emails: james.herterich@ucd.ie; frederic.dias@ucd.ie
[2]*CMLA, ENS Paris–Saclay, CNRS, Université Paris–Saclay, 94235 Cachan, France*
[3]*Earth Institute, University College Dublin, Belfield, Dublin 4, Ireland*

(*Received 15 May 2018*; *revised 28 February 2019*; *accepted 5 August 2019*; *first published online 5 September 2019*)

Steady two-dimensional fluid flow over an obstacle is solved using complex variable methods. We consider the cases of rectangular obstacles, such as large boulders, submerged in a potential flow. These may arise in geophysics, marine and civil engineering. Our models are applicable to initiation of motion that may result in subsequent transport. The local flow depends on the obstacle shape, slowing down in confining corners and speeding up in expanding corners. The flow generates hydrodynamic forces, drag and lift, and their associated moments, which differ around each face. Our model replaces the need for ill-defined drag and lift coefficients with geometry-dependent functions. We predict smaller flow velocities to initiate motion. We show how a joint-bound boulder can be transported against gravity, and analyse the influence of a wake region behind an isolated boulder.

Key words: Complex variable methods, conformal mapping, incompressible inviscid fluids, geophysics, fluid–solid interaction

2010 Mathematics Subject Classification: Primary: 86-08, 74F10; Secondary: 30C20, 76B99, 76D10

1 Introduction

Fluid flow around an obstacle is a classical problem in applied mathematics. In the literature, obstacles are often a protrusion (convex shaped) from a bottom rigid surface that is otherwise flat, over which there is a fluid flow. Obstacle shapes include semi-circles [26, 32, 33], ramps [2], triangles [1, 14, 25], step-downs [73] and other more complicated [11] and arbitrary topographies [10]. Well-like (concave shaped) obstacles [73], suspended obstacles in the flow [71], multiple fluid layers [10] and separating flows [73] have also been considered. Many of the above references contain a free surface, where there is often subcritical flow upstream and supercritical flow downstream, connected by a hydraulic fall. The Froude number plays an important role in the free-surface dynamics.

Fluid flow around an obstacle is typically not laminar, but well known to exhibit boundary-layer separation [64, 66]. Experiments of a turbulent boundary-layer flow over a step-up exhibit separated recirculating layers in front of and above the step, with reattachment position increasing with Reynolds number [62]. Potential flows can be modified to include separated

https://doi.org/10.1017/S0956792519000214 Published online by Cambridge University Press

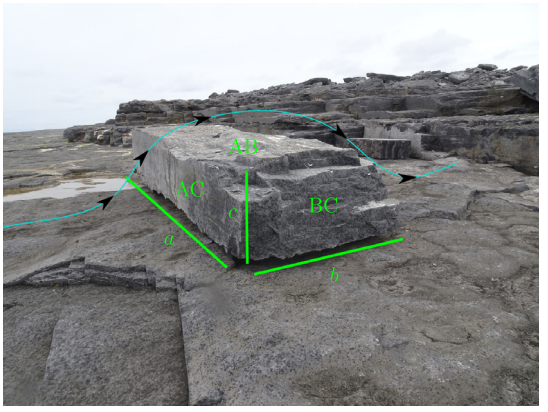


FIGURE 1. A fractured boulder on the Aran Islands, Ireland. The location is 16 m above high water, and 166 m inland at coordinates 53.0710° N, 9.6171° W. The slab has dimensions 5.7 m × 2.0 m × 0.8 m, and mass 22.3 t. The A-, B- and C-axes of lengths a, b and c, respectively, are indicated in green, as well as the faces. The typical flow direction, normal to the A-axis, is shown in blue. Photo by R. Cox (Williams College).

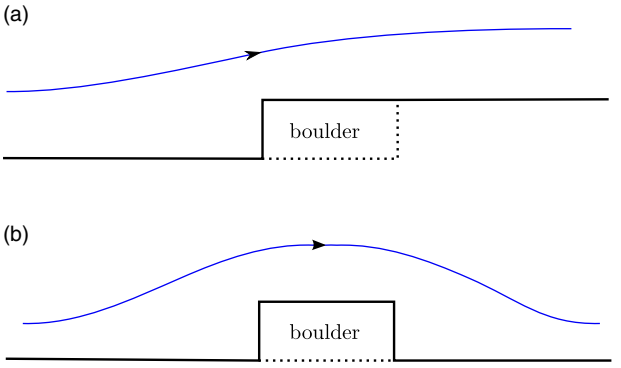


FIGURE 2. Schematic of the flow over (a) a boulder lodged against a step and (b) an isolated boulder. The solid lines are the rigid surfaces over which the fluid flows (arrows), and the dashed lines are the non-exposed surfaces of the boulder.

regions based on doublets and vortex pairs [73], overcoming *D'Alembert's paradox* [43]. However, potential source-vortex and doublet flows are stable to two-dimensional (2D) perturbations if the flow is inviscid, but unstable to three-dimensional (3D) perturbations [63]. For circular obstacles, as the Reynolds number increases, the point of separation moves downstream and the drag force is reduced. This is known as the *drag crisis* [42]. An analogous *lift crisis* occurs for non-symmetric (up-down) obstacles [13]. Potential flow is equivalent to an infinite Reynolds number flow. However, for rectangular bodies, as we will discuss, the sharp corners mean that separation is determined by the geometry itself [42]. For a surface-mounted cube, the wake is much larger behind the cube than to either side of and/or above it [41].

We consider this problem with large surface-mounted rectangular obstacles that may be transported by the flow. Some surfaces are in contact with the rigid bottom, but not attached

https://doi.org/10.1017/S0956792519000214 Published online by Cambridge University Press

(Figures 1 and 2). The context of this research is in coastal boulder transport. Coastal boulder deposits and cliff-top storm deposits occur worldwide and are well documented, for example, in Ireland [19, 20], Scotland [36], France [31], Malta [12], Hawaii [53], Japan [35] and the Philippines [48]. An example of a boulder fractured from the bedrock on the Aran Islands (Ireland) is shown in Figure 1.

Powerful amplified waves reach and overtop cliffs, and still retain the energy to transport boulders [61]. These include very large boulders (VLBs) greater than 100 tonnes, up to 40 m above the high-water mark, and 250 m inland from the high-water line [20]. Small boulders on low-lying platforms can be transported hundreds of metres by tidal currents [22]. Simulations show that long waves in the ocean are amplified by interactions with cliffs [5, 6, 75] and bathymetry [39]. Green water flows are characterised in the literature [58, 59].

There is debate over the types of waves that can cause VLB movement, storms or tsunamis. There are many arguments in favour of each theory. It is suggested that longer period waves (tsunamis) exert a longer sustained period of force on the boulder [35, 78], and that the force is larger than storms [60]. Alternatively, storms have a higher frequency [79] and within each storm there are more waves with (cumulatively) a greater total of energy than some tsunamis [77]. The evidence clearly suggests that both storms and tsunamis cause boulder movement, with long-term deposit organisation depending on the type of wave [60, 77].

Models of wave-induced boulder transport consider the forces applied to the boulder surface by the fluid flow [51, 55]. However, there is a limited understanding of the hydrodynamics for boulder extraction and transport [18, 57]. The fluid flow around an obstacle is non-trivial, as already discussed, and generally not reducible to a single constant flow parameter, such as a depth-average velocity [52, 55] or oscillating with the wave motion [78]. In fact, the velocity component of the drag force is usually related to the depth-averaged velocity, but the lift force is related to the bed velocity, which is turbulent and can differ by 20% [55]. This is important in river beds, where the averaged boundary shear stress forms the critical Shields parameter, for incipient motion of small particles forming a rough surface [76]. The drag coefficient also depends on the Reynolds number of the flow [42, 45]. In unsteady flow, the impulse generated during large but brief forces may initiate motion [7, 21].

In this paper, we address the non-trivial flow and hydrodynamic forces around a submerged obstacle. We consider a 2D potential flow that is uniform in the far field. We formulate the problem in complex variable terms using conformal mappings to a geometry in which the flow is simple. We consider two situations representing observed large boulder placements, lodged against a platform step and stand-alone on a platform (Figures 1 and 2). The joint-bound boulder we consider represents a fractured boulder from the bedrock to be extracted and transported, or that has been transported to a natural platform step [19, 38]. It has an exposed front AC-face and top AB-face. Other forms of joint-bound boulders exist, such as on exposed on the top surface [55]. The isolated boulder represents a stand-alone VLB to be transported, with two AC-faces and the top AB-face exposed to the flow.

Finally, we reformulate the boulder transport equations, taking into account the difference in flow, forces and moments on each side of the boulder. However, we only consider initiation of motion, where hydrodynamic forces acting on a static boulder balance body and contact forces. Once motion begins, the pressure on the surface changes rapidly, a situation beyond steady potential flow theory. Notation is summarised in Appendix A.

https://doi.org/10.1017/S0956792519000214 Published online by Cambridge University Press

2 Theory

2.1 Potential flow

We analyse 2D steady, inviscid, incompressible, irrotational flow around a submerged obstacle such as a boulder. Incompressibility and irrotationality mean that the velocity components (u, v) may be written as derivatives of two potential functions

$$u(x,y) = \frac{\partial \Phi(x,y)}{\partial x} = \frac{\partial \Psi(x,y)}{\partial y}, \tag{2.1a}$$

$$v(x,y) = \frac{\partial \Phi(x,y)}{\partial y} = -\frac{\partial \Psi(x,y)}{\partial x}, \tag{2.1b}$$

where $\Phi(x,y)$ is the velocity potential and $\Psi(x,y)$ is the stream function, each satisfying Laplace's equation

$$\nabla^2 \Phi = 0, \qquad \nabla^2 \Psi = 0,$$

in the fluid domain and together satisfy the Cauchy–Riemann equations [4, 16]. Hence the complex potential

$$w(z) = \Phi + i\Psi \tag{2.2}$$

is a holomorphic function of $z = x + iy$, such that

$$\frac{\mathrm{d}w(z)}{\mathrm{d}z} = u(x,y) - iv(x,y). \tag{2.3}$$

The pressure $p(x,y)$ is given by Bernoulli's equation

$$p + \frac{1}{2}\rho\,(u^2 + v^2) = \text{constant}, \tag{2.4}$$

where gravity is neglected and ρ is the constant density of the fluid [9]. We impose an impenetrable (rigid) wall boundary condition

$$\mathrm{Im}\, w = 0. \tag{2.5}$$

We use these properties for a standard conformal mapping approach to flow over boulders as in Figure 2. Flow over such boulders include expansion ($>\pi$ rad) corners. Here, potential flow results in local singularities. Although one may reasonably expect the flow to be large here, it is finite. We will address this drawback directly as it appears.

2.2 Conformal mapping

Solving for the flow around an obstacle is challenging due to the complex geometries involved, even in ideal cases where the obstacles are blocks with straight edges. We solve Laplace's equation for the flow using conformal (angle preserving) mapping techniques. In this way, we can transform an inconvenient geometry to a convenient one, that is, in which the solution to Laplace's equation is simple. The inverse mapping provides the solution in the original domain. We consider mappings between the physical domain D (the region above the rigid boundaries in Figure 2) and the upper-half plane (UHP).

https://doi.org/10.1017/S0956792519000214 Published online by Cambridge University Press

For a polygonal geometry (including a vertex at infinity), we use the Schwarz–Christoffel formula [27, 50]. This has been used extensively for potential flow problems such as jets [24] and flows involving polygonal obstacles [29]. Numerical computations have been researched extensively [69]. In this paper, we approach the problem analytically, until such times as an integral must be computed numerically. Each vertex of the polygon in physical space has an interior angle $\alpha\pi$ rad and exterior angle $\beta\pi$ rad, with $\alpha + \beta = 1$ and $-2 \leqslant \beta \leqslant 2$. As we circumnavigate the polygon, $\beta > 0$ when turning left, $\beta < 0$ when turning right. Furthermore, each vertex in the physical plane $z = x + iy$ is associated with a point on the real line ξ (with $\xi_1 < \xi_2 < \dots$) of the UHP $\zeta = \xi + i\eta$ ($\eta \geqslant 0$). The Schwarz–Christoffel mapping from the UHP to an $n-1$ point polygon (with an nth vertex at infinity) is given by

$$z = f(\zeta) = A + B \int^{\zeta} \prod_{j=1}^{n-1} (t - \xi_j)^{-\beta_j} \, \mathrm{d}t, \tag{2.6}$$

where the constants A and B fix the location and rotation or scaling of the polygon. The Riemann mapping theorem allows us to use at most three vertices on the polygon to fix the geometry, with the other points uniquely defined by the mapping [56].

For rectangular geometries, $\beta_j = \pm 1/2$. We always choose the branch such that $(x - x_j)^{\pm 1/2}$ is positive for $x > x_j$ as is usual [29]. In general, we consider the principal branches of complex-valued multifunctions.

The complex potential $w(z)$ (2.2) in physical space D has a corresponding complex potential $\omega(\zeta)$ in conformal space in the UHP. As Laplace's equation is conformally invariant [56], the real and imaginary components of ω satisfy Laplace's equation in $f^{-1}(D)$. We solve the problem in conformal space, and recover the complex potential solution in physical space by

$$w(z) = \omega(\zeta) = \omega\left(f^{-1}(z)\right). \tag{2.7}$$

We define the flow speed from the complex velocity (2.3) as

$$U = \left(u^2 + v^2\right)^{\frac{1}{2}}. \tag{2.8}$$

The flow at the boulder surface is along a finite length of the ξ axis. The conformal map to the boulder surface in physical space is non-linear, influenced by the shape (size and aspect ratio) of the boulder. For our special case of rectangular boulders, the mapping is segmented into regions of constant y and constant x along the faces of the boulder.

2.3 Classical forces on a boulder

Fluid flow past a body exerts hydrodynamic forces such as drag and lift. We consider boulders with length, width and height along the A-, B- and C-axes sides of length a, b, c, respectively (Figure 1). Typically, $a > b > c$ with the flow normal to the A-axis [54]. Though hydrodynamic moments generate this orientation [36], it requires large transport distances and so is considered a guide. In Figure 2, we show flow over the B- and C-axes, with the longer A-axis into the page. The forces take the form

$$F_d = \frac{1}{2} \rho \, C_d \, ac \, V^2, \tag{2.9a}$$

$$F_l = \frac{1}{2} \rho \, C_l \, ab \, V^2, \tag{2.9b}$$

https://doi.org/10.1017/S0956792519000214 Published online by Cambridge University Press

where C_d and C_l are the coefficients of drag and lift, respectively, and V is a measure of the fluid velocity, often the depth-average velocity [52, 55]. Importantly, these forces depend on V^2, called *quadratic drag*. Whereas models exist using different coefficients and surface areas, that is, $ab \to a(b+c)$ in the lift force [49], quadratic drag is used in all models for high velocity flows. When the boulder is in motion, the forces depend on the relative velocity $(V - U_b)^2$, where U_b is the boulder velocity [52]. Furthermore, boulder motion induces an inertia force

$$F_m = \rho\, C_m\, abc\, \left(\dot{V} - \dot{U}_b\right), \tag{2.10}$$

where $\dot{V}$ and $\dot{U}_b$ are the instantaneous flow and boulder accelerations [55].

The boulders are also subject to body and contact forces that resist movement. The gravitational and (Coulomb) friction forces are given by

$$F_g = (\rho_s - \rho)\, g\, abc, \tag{2.11a}$$

$$F_f = \mu\, \left(F_g - F_l\right), \tag{2.11b}$$

respectively, where ρ_s is the density of the boulder, g is the acceleration due to gravity and μ is the coefficient of (static) friction [51]. Dynamic friction is incorporated when the boulders are moving [45].

Each force on the boulder generates a moment [51], typically given by

$$M_d = \frac{c}{2}F_d, \qquad M_l = \frac{b}{2}F_l, \qquad M_m = \frac{c}{2}F_m, \qquad M_g = \frac{b}{2}F_g. \tag{2.12}$$

These are rotational forces on the boulder.

Boulders are found in different states: submerged, sub-aerial, joint bound, etc. [51]. We consider the submerged case only. The hydrodynamic forces (2.9) must overcome the body and contact forces (2.11), and/or their associated moments, for boulder transport to occur. For a submerged boulder on a flat platform, motion occurs via *sliding*, *rolling* and *saltation* [45]. Each type occurs when different criteria are met. Sliding occurs when the drag force (2.9a) overcomes the friction force (2.11b) to translate the boulder along the surface with one side in constant contact with the platform. Rolling (or overturning) occurs when the drag and lift moments exceed the gravitational restraining moment (2.12) to roll the boulder along the platform. Saltation occurs when the lift force (2.9b) exceeds the gravitational force (2.11a), with the boulder no longer in contact with the platform, allowing for transport by the flow. These are summarised [51] as follows:

$$F_d > F_f \quad \text{(sliding)}, \tag{2.13a}$$

$$M_d + M_l > M_g \quad \text{(rolling)}, \tag{2.13b}$$

$$F_l > F_g \quad \text{(saltation)}. \tag{2.13c}$$

We neglect F_m and M_m as we assume the boulder to be stationary and consider initiation of motion only. The subsequent motion is more complicated with transient oscillations and inertial effects [30]. As sliding, rolling and saltation refer to types of sustained transport, we will refer to the initiation of motion process for each as *nudging*, *overturning* and *lift*, respectively. However, it makes sense to keep the same force and moment balance conditions (2.13) to model the occurrence of each. For later comparison, we solve for the flow velocity V required to move a boulder by models in the literature

https://doi.org/10.1017/S0956792519000214 Published online by Cambridge University Press

$$V^2 > 2\mu g \frac{\rho_s - \rho}{\rho} \frac{b}{C_d + \mu \frac{b}{c} C_l} \quad \text{(sliding)}, \tag{2.14a}$$

$$V^2 > 2g \frac{\rho_s - \rho}{\rho} \frac{b^2}{c\left(C_d + \frac{b^2}{c^2} C_l\right)} \quad \text{(rolling)}, \tag{2.14b}$$

$$V^2 > 2g \frac{\rho_s - \rho}{\rho} \frac{c}{C_l} \quad \text{(saltation)}, \tag{2.14c}$$

via (2.9), (2.11), (2.12) and 2.13).

As stated, the hydrodynamic forces (2.9) depend on a measure of the fluid velocity V. In most models (including those cited above), this velocity is taken as a depth-averaged velocity. Although the disturbance to the flow by the boulder is felt throughout the fluid, the disturbance is greatest at the boulder surface itself and decays rapidly with distance [4]. As such, the depth-averaged flow is inadequate for calculating the hydrodynamic forces. Furthermore, the drag and lift coefficients are ill-defined for many boulder situations and flows [57].

In this paper, we determine the flow around the boulder, in a number of situations, using complex variable techniques. We calculate the point-wise flow around the boulder, and hence the forces. Implicit in these calculations are the drag and lift coefficients. We see them later as geometry-dependent functions, and we compare the two results.

2.4 Complex forces on a boulder

The forces from a steady potential flow can be computed directly from the complex potential. In Appendix B, we use Blasius's theorem to relate the net drag F_d and lift F_l forces to an integral around an obstacle's boundary [4]. We deduce that

$$F_d - i F_l = -\frac{1}{2} i \rho a \int_{C_\zeta} \left[\left(\frac{\mathrm{d}\omega}{\mathrm{d}\zeta} \right)^2 \Big/ \frac{\mathrm{d}z}{\mathrm{d}\zeta} \right] \mathrm{d}\zeta, \tag{2.15}$$

where C_ζ is the exposed boundary in the ζ-plane. The factor a, the length of the boulder, accounts for 3D effects. We integrate in the clockwise direction (increasing ζ) around the obstacle, and thus include an additional minus sign. Although singularities are present in the flow, these integrals converge.

Similarly, the moment of the force can be expressed [4] as

$$M = \mathrm{Re}\left\{ \frac{1}{2} \rho a \int_{C_\zeta} \left[f(\zeta) \left(\frac{\mathrm{d}\omega}{\mathrm{d}\zeta} \right)^2 \Big/ \frac{\mathrm{d}z}{\mathrm{d}\zeta} \right] \mathrm{d}\zeta \right\}, \tag{2.16}$$

using $z = f(\zeta)$ (2.6). Again, the expression is corrected for 3D effects and clockwise (increasing ζ) integration.

2.5 D'Alembert's paradox

The hydrodynamic forces discussed in the previous section depend on the flow. However, potential flow around an obstacle, in theory, does not generate any drag force. Yet, in experimental set-ups of potential flow, there is significant drag. This inconsistency is known as D'Alembert's paradox [4].

https://doi.org/10.1017/S0956792519000214 Published online by Cambridge University Press

D'Alembert's paradox is resolved via viscous–inviscid interactions. Potential flows do not satisfy the no-slip boundary condition [46]. Viscous–inviscid interactions are resolved through matched asymptotic expansions near singular boundary-layer separation points for bluff bodies [65], rigid bodies [68] and airfoils [72]. In airfoil theory, irrotational and circulation-free flow results in infinite velocity at a trailing edge. The boundary conditions are satisfied by imposing a Kutta condition. This *ad hoc* condition imposes a finite velocity, a viscous effect, through circulation. However, the underlying momentum equations are inviscid [4, 73].

The Kutta condition may be bypassed by imposing a flow angle at the boundaries that we can determine *a priori*. Here the generalised Poisson Integral Formula generates a separated recirculating region, an analytic function, related to the flow in the complex plane [73, 74].

2.6 Parameter values

We consider a flow of water over limestone, a common VLB rock type. The density of water is $\rho = 1000\,\mathrm{kg/m^3}$, and the maximum density of limestone is $\rho_s = 2560\,\mathrm{kg/m^3}$, so that $\rho_s/\rho = 2.56$ [20]. The boulder dimensions are typically $a = 2$–$5\,\mathrm{m}$, $b = 1$–$3\,\mathrm{m}$, and $c = 0.5$–$1\,\mathrm{m}$ [19]. The fluid velocity U_∞ depends on the situation, from 10 cm/s for tidal currents to 10 m/s for tsunami inundations. The acceleration due to gravity is $g = 9.8\,\mathrm{m/s^2}$.

Coefficients for hydrodynamic and contact forces can vary depending on the object shape and properties of the flow [40]. However, certain values have become prevalent, such as a drag range $C_d = 1$–2, $C_l = 0.178$ and $\mu = 0.55$ [52]. The drag coefficient is known to depend on shape [17, 37] and can vary $C_d = 1$–3 in a turbulent flow [41]. This specific lift coefficient has a long history, originally based on experiments [28] using coarse particles (6.9 cm spheres) and calculating the velocity around the spheres [17, 37]. This value has been criticised in the literature as unrealistic, suggesting much larger values mostly distributed in the range $C_l = 2 - 3$ [57].

3 Joint-bound boulder

3.1 Set-up

We model the flow over a boulder lodged against a stepped platform (Figure 2 (a)). For simplicity, we assume that the boulder and platform form a continuous boundary that is smooth at the point of separation. The boulder and the step have the same height c. In this way, the flow implicitly recognises the boulder, with the whole system simply a converging step. We can vary the width b of the boulder by the distance outwards from the step (Figure 3). The four corners of the boulder are taken to be $(x, y) = (0, 0), (0, c), (b, c), (b, 0)$, with only the sides $(0, 0)$ to $(0, c)$ and $(0, c)$ to (b, c) exposed to the flow. The polygonal region is defined by the two corners $(x, y) = (0, 0)$ and $(0, c)$ that form the step, and a point at infinity. In the far field, the flow is uniform:

$$(u, v) = (U_\infty, 0). \tag{3.1}$$

3.2 Mapping and flow

We map the UHP to the stepped polygonal region via the correspondence

$$\xi_1 = -1 \longleftrightarrow 0 = z_1, \qquad \xi_2 = 1 \longleftrightarrow ic = z_2, \tag{3.2}$$

https://doi.org/10.1017/S0956792519000214 Published online by Cambridge University Press

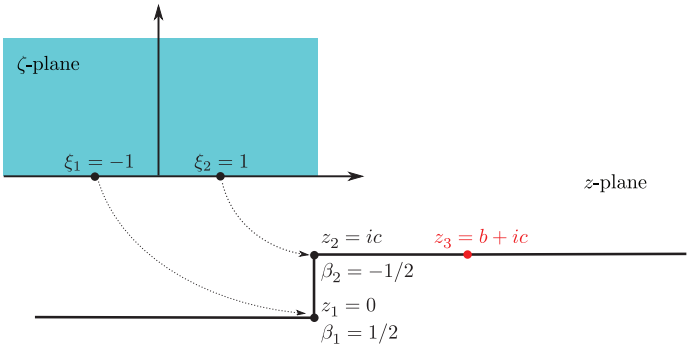


FIGURE 3. The UHP in the ζ-space is mapped conformally to the polygonal step in z-space by the Schwarz–Christoffel map $z = f(\zeta)$ (3.3) using the vertex points z_j and exterior angles β_j. The exposed boulder faces are the straight line segments between $[z_1, z_2]$ (the AC-face) and $[z_2, z_3]$ (the AB-face).

where the exterior angles are $\beta_1 = 1/2$ and $\beta_2 = -1/2$, respectively (Figure 3). The Schwarz–Christoffel map (2.6) is given by

$$z = x + iy = f(\zeta) = ic + \frac{c}{\pi}\left(\sqrt{\zeta^2 - 1} - \cosh^{-1}(\zeta)\right). \tag{3.3}$$

See Appendix C for details. This is a well-known solution [44].

The associated complex potential in conformal space (Appendix C) takes the form

$$\omega = \frac{U_\infty c \zeta}{\pi}, \tag{3.4}$$

with velocity components (2.3)

$$u - iv = \frac{\mathrm{d}w}{\mathrm{d}z} = \frac{\mathrm{d}\omega}{\mathrm{d}\zeta} \Big/ \frac{\mathrm{d}z}{\mathrm{d}\zeta} = U_\infty \sqrt{\frac{\zeta + 1}{\zeta - 1}}. \tag{3.5}$$

We note that the velocity is zero at the foot ($\zeta = -1$) of the step and infinite at the top ($\zeta = 1$) corner (Figure 4). This local singularity is expected in potential flow around an expansion ($> \pi$ rad) corner. With the mapping (3.3) and velocity (3.5), we compute the flow speed $U = \sqrt{u^2 + v^2}$ (2.8) at any point around the boulder. The flow in conformal space does not depend on the size of the boulder. The real values of ζ correspond to the solid boundary; specifically $\zeta = \xi \in (-1, 1)$ the step face, and $\zeta = \xi \in (1, f^{-1}(b + ic))$ the top face of the boulder (Figure 3). As $|\xi|$ increases, $U \to U_\infty$.

It is the non-linear mapping (3.3) to physical z-space that determines the flow disturbance with respect to a particular step height c. The higher the step height, the greater the disturbance, as evident by the scaling of c in (3.3). Approaching the step, the disturbance is a reduction in flow speed ($U < U_\infty$). Along the step (AC-face), the flow speed increases from zero at the bottom corner to infinity at the top corner. The flow is given by $U = U_\infty$ at $\zeta = 0$ (2.8) and (3.5), occurring at $z = ic\,(1 + (1 - \pi/2)/\pi) \approx i\,0.81831c$ (3.3). Beyond the step, the speed decreases ($U > U_\infty$). The disturbance decays with distance to the uniform background flow.

https://doi.org/10.1017/S0956792519000214 Published online by Cambridge University Press

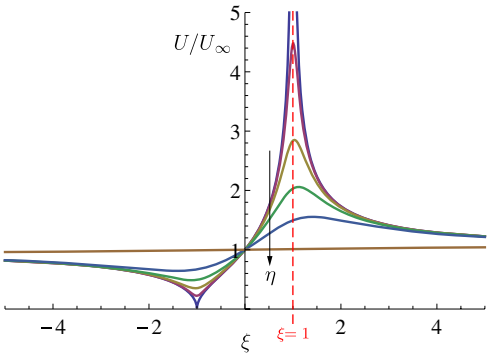


FIGURE 4. Flow speed U (2.8) and (3.5), normalised by background flow U_∞, in conformal space against ξ for $\eta = \{0, 0.1, 0.25, 0.5, 1, 10\}$. The arrow indicates increasing values of η. Further away from the boulder, as $|\xi|$ and η increase, $U \to U_\infty$. Along the boulder surface ($\eta = 0$), the speed is zero at the $\pi/2$ rad bottom corner of the step ($\xi = -1$) and infinite at the $-\pi/2$ rad top corner ($\xi = 1$), with the step face in the region $\xi \in (-1, 1)$, $\eta = 0$ (Figure 3).

3.3 Forces and moments

The forces on the AC ($\xi \in (-1, 1), \eta = 0$) and AB ($\xi \in (1, f^{-1}(b)), \eta = 0$) faces of the boulder are non-trivial, due to the form of the flow (3.5). We substitute the mapping (3.3) and flow (3.5) into the expression for the forces (2.15), giving

$$F_d^{\mathrm{AC}} - i\,F_l^{\mathrm{AC}} = -\frac{1}{2} ia\rho \frac{cU_\infty^2}{\pi} \int_{-1}^{1} \sqrt{\frac{\zeta+1}{\zeta-1}}\,\mathrm{d}\zeta = \frac{1}{2}\rho acU_\infty^2, \tag{3.6a}$$

$$F_d^{\mathrm{AB}} - i\,F_l^{\mathrm{AB}} = -\frac{1}{2} ia\rho \frac{cU_\infty^2}{\pi} \int_{1}^{\xi_3} \sqrt{\frac{\zeta+1}{\zeta-1}}\,\mathrm{d}\zeta = -i\,\frac{1}{2}\rho acU_\infty^2 \Theta_F(\xi_3), \tag{3.6b}$$

where $\xi_3 = f^{-1}(b + ic)$ (3.3) is the ζ-plane value of the $z_3 = b + ic$ edge of the boulder (Figures 2 (a) and 3). The function $\Theta_F(\xi_3) = -i\left(\sin^{-1}\xi_3 - \sqrt{1-\xi_3^2}\right)$ is a positive, increasing, real-valued function for $\xi_3 > 1$, that tends to a linear function (Figure 5). There is no lift on the AC face and no drag on the AB face. The lift force (3.6b) exceeds the drag force (3.6),

$$\frac{F_l}{F_d} = \Theta_F\,(\xi_3), \tag{3.7}$$

as b/c becomes larger (Figure 5), with equality at $b/c \approx 0.14$.

To compare the hydrodynamic forces (3.6) with expressions in the literature (2.9), we consider the correspondence

$$F_d = \frac{1}{2}\,\rho\,C_d\,ac\,V^2 \longleftrightarrow \frac{1}{2}\rho\,ac\,U_\infty^2, \tag{3.8a}$$

$$F_l = \frac{1}{2}\,\rho\,C_l\,ab\,V^2 \longleftrightarrow \frac{1}{2}\rho\,ac\,U_\infty^2\Theta_F\,(\xi_3)\,. \tag{3.8b}$$

https://doi.org/10.1017/S0956792519000214 Published online by Cambridge University Press

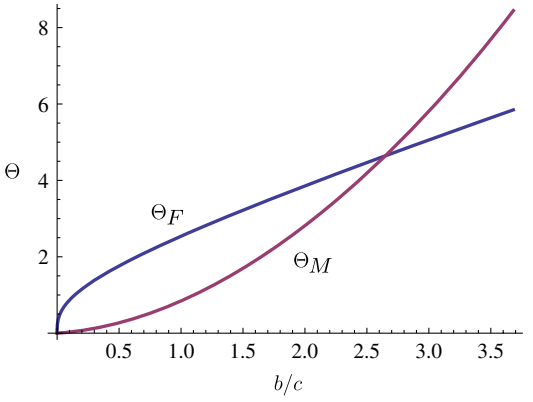


FIGURE 5. Functions for the lift force and moment: Θ_F (3.6b) in the lift force and Θ_M (3.10b) in the lift moment for a joint-bound boulder against aspect ratio b/c.

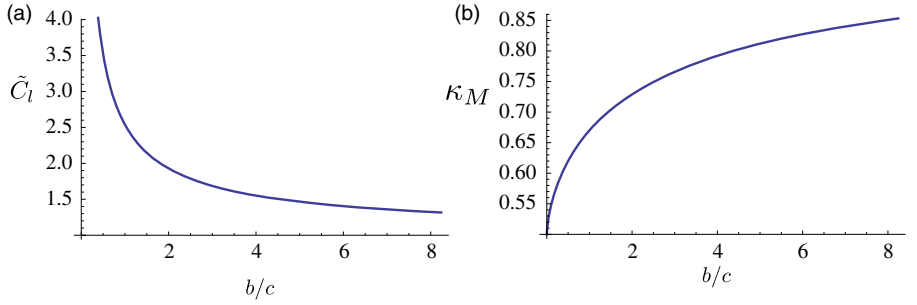


FIGURE 6. Lift force and moment factors compared to literature for a joint-bound boulder in a potential flow depend on the geometry, shown here as a function of boulder aspect ratio b/c. (a) Derived geometry-dependent lift coefficient $\tilde{C}_l = \frac{c}{b}\,\Theta_F\,(\xi_3)$ (3.9b) and (b) lift moment scaling factor $\kappa_M = 2\frac{c}{b}\frac{\Theta_M(\xi_3)}{\Theta_F(\xi_3)}$ (3.13) compared to the literature.

By comparison, and equivalating V with U_∞, we deduce expressions for the drag and lift coefficients,

$$C_d \longleftrightarrow 1 =: \tilde{C}_d, \tag{3.9a}$$

$$C_l \longleftrightarrow \frac{c}{b}\,\Theta_F\,(\xi_3) =: \tilde{C}_l. \tag{3.9b}$$

The drag coefficient is set to 1 but lift coefficient depends on the geometry via the aspect ratio b/c (Figure 6 (a)). The lift coefficient $\tilde{C}_l$ decreases to a constant as b/c increases. The flow disturbance above the boulder decreases with distance (Figure 4). A larger b/c means the flow, and hence lift, on the top surface is on average smaller. Hence, the decrease in $\tilde{C}_l$. However, though the values are an order of magnitude greater than the often reported $C_l = 0.178$ in the literature (cf. Section 2.6), it is in the predicted range of [57].

The moments of the force (2.16) are given by

$$M_d = \mathrm{Re}\left\{\frac{1}{2}\rho a c^2 U_\infty^2 \int_{-1}^{1} \frac{1}{\pi}\left[i + \frac{1}{\pi}\left(\sqrt{\zeta^2-1} - \cosh^{-1}(\zeta)\right)\right]\sqrt{\frac{\zeta+1}{\zeta-1}}\,\mathrm{d}\zeta\right\}$$

$$\approx \frac{1.81}{4}\rho a c^2 U_\infty^2, \tag{3.10a}$$

https://doi.org/10.1017/S0956792519000214 Published online by Cambridge University Press

$$M_l = \mathrm{Re}\left\{\frac{1}{2}\rho a c^2 U_\infty^2 \int_1^{\xi_3} \frac{1}{\pi}\left[i + \frac{1}{\pi}\left(\sqrt{\zeta^2-1} - \cosh^{-1}(\zeta)\right)\right]\sqrt{\frac{\zeta+1}{\zeta-1}}\,\mathrm{d}\zeta\right\}$$
$$= \frac{1}{2}\rho a c^2 U_\infty^2 \Theta_M(\xi_3), \tag{3.10b}$$

using (3.3) and (3.5). Again, $\xi_3 = f^{-1}(b + ic)$ (3.3). The lift moment (3.10b) increases with aspect ratio b/c according to a positive increasing function Θ_M that is the real value of the integral (Figure 5). The lift moment exceeds the drag moment as b/c increases,

$$\frac{M_l}{M_d} = \frac{2}{1.81}\Theta_M\,(\xi_3), \tag{3.11}$$

as b/c becomes larger (Figure 5). Here, equality occurs at $b/c \approx 1.037$, where the B- and C-axes are approximately equal. The moments (3.10) correspond to those given in the literature (2.12) by

$$M_d = \frac{1}{4}\,\rho\, C_d\, a c^2\, V^2 \longleftrightarrow \frac{1.81}{4}\rho a c^2 U_\infty^2, \tag{3.12a}$$

$$M_l = \frac{1}{4}\,\rho\, C_l\, a b^2\, V^2 \longleftrightarrow \frac{1}{2}\rho a c^2 U_\infty^2 \Theta_M\,(\xi_3). \tag{3.12b}$$

Given the correspondences for the forces (3.8) and (3.9), the drag moment is proportionally greater (by factor of 1.81) than the scaling of the moment given in the literature. The lift moment scales non-trivially by a scaling factor

$$\kappa_M = 2\frac{c}{b}\frac{\Theta_M\,(\xi_3)}{\Theta_F\,(\xi_3)}, \tag{3.13}$$

that depends on the boulder aspect ratio b/c, shown in Figure 6 (b). The factor is less than one for all reasonable boulder aspect ratios. Hence, compared to models in the literature, the flow around a joint-bound boulder contributes more towards the drag moment than the lift moment. Therefore, overturning against gravity up the step is generated more by the drag moment than lift moment.

3.4 Initiation of motion

3.4.1 *Motion type*

The boulder can only be moved up and over step, by overturning or lift. The geometric constraints (Figure 2 (a)) of a joint-bound boulder mean that sliding cannot occur, regardless of the drag force.

The most common explanation for boulder motion against gravity is overturning (2.13b). The drag and lift moments (3.10) exceed the gravitational moment (2.12) when

$$\frac{M_d + M_l}{M_g} = \frac{U_\infty^2 c\,(0.905 + \Theta_M(\xi_3))}{b^2 g\left(\frac{\rho_s}{\rho} - 1\right)} > 1. \tag{3.14}$$

https://doi.org/10.1017/S0956792519000214 Published online by Cambridge University Press

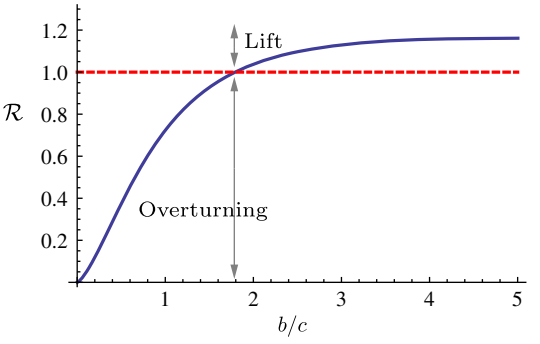


FIGURE 7. Motion criteria ratio $\mathcal{R}$ (3.16) against boulder aspect ratio b/c. Lift occurs when the ratio is $\mathcal{R} > 1$, and overturning when $\mathcal{R} < 1$. The dashed line is $\mathcal{R} = 1$.

The lift force (3.6b) exceeds the restraining force due to gravity (2.11a) when

$$\frac{F_l}{F_g} = \frac{U_\infty^2 \Theta_F(\xi_3)}{2bg\left(\frac{\rho_s}{\rho} - 1\right)} > 1, \tag{3.15}$$

resulting in lift (2.13c). If lift does occur, it does not mean that it can lift the boulder a vertical distance c up the step. Hydrodynamic forces and moments from underneath the boulder will become significant, as will dynamic pressures and inertial forces [8, 67].

We now consider which criteria is first exceeded, overturning (3.14) or lift (3.15). We define the ratio

$$\mathcal{R} = \frac{F_l}{F_g} \Big/ \frac{M_d + M_l}{M_g} = \frac{b\,\Theta_F(\xi_3)}{2c\,(0.905 + \Theta_M(\xi_3))} = \begin{cases} < 1 & \text{(overturning)}, \\ > 1 & \text{(lift)}. \end{cases} \tag{3.16}$$

Lift occurs first for $\mathcal{R} > 1$ and overturning for $\mathcal{R} < 1$. This is a purely geometrical relationship, with results summarised in Figure 7. Should transport occur, then for an aspect ratio $b/c < 1.793$, overturning is more likely to occur first, while for $b/c > 1.793$, lift is most likely. This makes sense as it corresponds to a larger AB-face area for the lift force and a larger B-axis to rotate about (Figure 1).

3.4.2 *Velocity*

We can write the criteria for initiation of motion (3.14) and (3.15) in terms of a velocity threshold to predict motion

$$U_\infty^2 > g\frac{\rho_s - \rho}{\rho}\frac{b^2}{c\,(0.905 + \Theta_M(\xi_3))} \quad \text{(overturning)}, \tag{3.17a}$$

$$U_\infty^2 > 2g\frac{\rho_s - \rho}{\rho}\frac{b}{\Theta_F(\xi_3)} \quad \text{(lift)}. \tag{3.17b}$$

In our model, this represents the constant background velocity of the potential flow that varies locally around the obstacle. The velocities depend on gravity, densities and geometry. Predicted threshold velocities for different geometries are shown in Figure 8. We find a pessimal boulder geometry exists for overturning such that the predicted velocity to initiate motion is maximised

https://doi.org/10.1017/S0956792519000214 Published online by Cambridge University Press

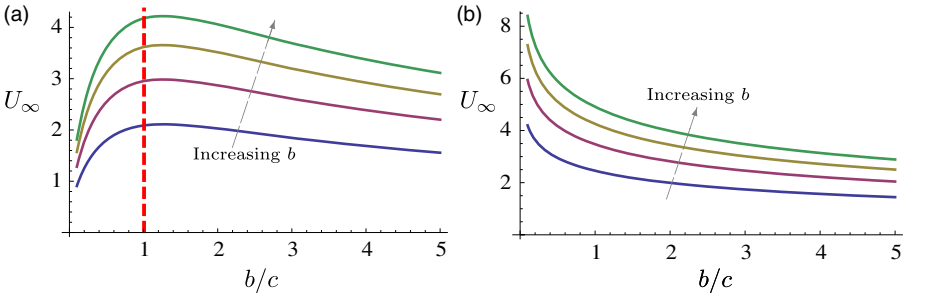


FIGURE 8. Predicted background velocity in m/s for initiation of motion. (a) Overturning U_∞ (3.17a). (b) Lift U_∞ (3.17b). The B-axis length $b = \{0.5\,,\,1\,,\,1.5, 2\,\text{m}\}$ value increases with each curve, plotted against b/c. Other parameters are given in Section 2.6. The dashed line in (a) denotes $b/c = 1$, when the 2D profile is rectangular.

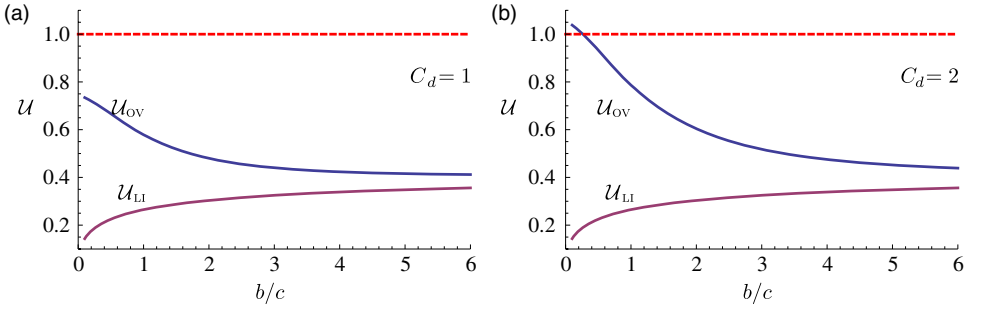


FIGURE 9. Ratio of critical velocities $\mathcal{U}$ (3.18) to initiate boulder transport with (a) $C_d = 1$ and (b) $C_d = 2$. Other parameter values are given in Section 2.6. The dashed red line is $\mathcal{U} = 1$ above which models in the literature require a smaller velocity to initiate transport, below which our model requires a smaller velocity.

(Figure 8 (a)). This is a near-rectangular shape and coincides with our earlier observation of approximately equal drag and lift moments for this geometry, cf. (3.11). The velocity required for lift (Figure 8 (b)) decreases with b/c as expected.

We now compare our predicted initiation of motion values (3.17) to those for models in the literature (2.14) by defining a ratio $\mathcal{U}$ such that

$$\mathcal{U} = \frac{U_\infty}{V} = \begin{cases} > 1, \\ < 1, \end{cases} \tag{3.18}$$

where $\mathcal{U} < 1$ means our model requires a lower velocity than in the literature for transport to occur, and *vice versa* for $\mathcal{U} > 1$. For overturning (OV) and lift (LI), this ratio is given by

$$\mathcal{U}^2_{\text{OV}} = \frac{C_d + \frac{b^2}{c^2} C_l}{1.81 + 2\Theta_M(\xi_3)}, \tag{3.19a}$$

$$\mathcal{U}^2_{\text{LI}} = \frac{b}{c} \frac{C_l}{\Theta_F(\xi_3)}. \tag{3.19b}$$

Using typical values given in Section 2.6, our model, in general, requires a smaller fluid velocity to initiate boulder transport, especially for lift (Figure 9). There is only a small range of aspect

https://doi.org/10.1017/S0956792519000214 Published online by Cambridge University Press

Table 1. *Examples of predicted velocities to initiate motion of a joint-bound boulder. Predicted transport velocities from the literature are calculated as V (2.14) and background flows from our potential-flow model are calculated as U_∞ (3.17). The boulder B- and C-axes are given by b and c, respectively*

b	c	b/c	Motion type	V	U_∞
1 m	1 m	1	Rolling/overturning	3.8 m/s	3.0 m/s
1 m	1 m	1	Saltation/lift	13.1 m/s	3.5 m/s
2 m	1 m	2	Rolling/overturning	6.8 m/s	4.1 m/s
2 m	1 m	2	Saltaton/lift	13.1 m/s	4.0 m/s

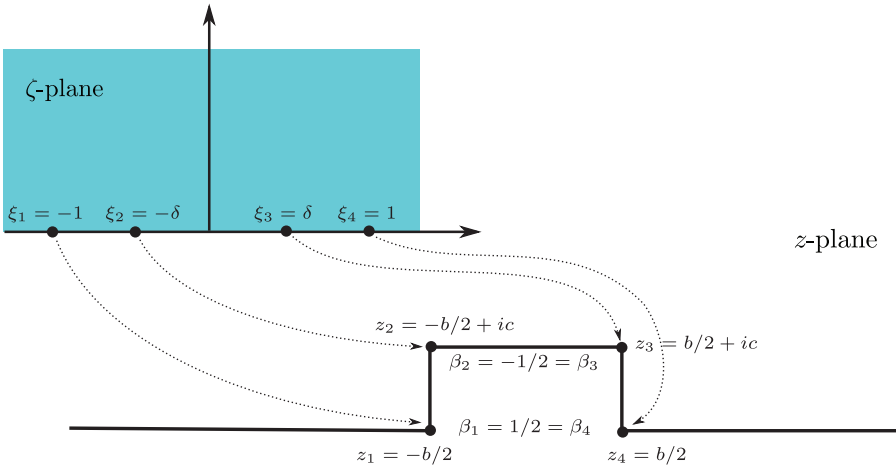


FIGURE 10. The UHP in the ζ-space is mapped conformally to the polygonal rectangle obstacle in z-space by the Schwarz–Christoffel map $z = f(\zeta)$ (4.2) using the vertex points z_j and exterior angles β_j. The exposed boulder faces are the straight line segments between $[z_1, z_2]$ (front AC-face), $[z_2, z_3]$ (AB-face) and $[z_3, z_4]$ (rear AC-face).

ratios, atypical of those observed in the field, at high drag coefficients, for which the models in the literature require a slower flow velocity. For large aspect ratios b/c, the velocity required is less than 1/2 of that previously expected. These differences, in dimensional numbers, are significant. In terms of submerged obstacles in strong currents, overturning and lift velocity thresholds are not only reduced (Figure 8 and Table 1), but are also comparable numbers to real flows. Typically, it was predicted that lift velocities needed to be much higher, beyond realistic values.

4 Isolated boulder

4.1 Set-up

We model the flow over an isolated boulder (Figure 2 (b)). Again, for simplicity we assume that the boulder and rigid platform form a continuous boundary that is smooth at the point of separation. The boulder has height c and width b (Figure 10). The four corners of the boulder are taken to be $(x, y) = (-b/2, 0), (-b/2, c), (b/2, c), (b/2, 0)$, with all sides but $(-b/2, 0)$ to $(b/2, 0)$

https://doi.org/10.1017/S0956792519000214 Published online by Cambridge University Press

exposed to the flow. The polygonal region is defined by all four corners, and a point at infinity. Again, we take uniform flow in the far field (3.1).

4.2 Mapping and flow

There are a number of ways to approach the conformal mapping between the UHP and a rectangular obstacle. The problem is more complicated (mathematically) than the step case, arising from the choice and number of prevertices, and the geometry (aspect ratio) of the boulder. We consider a parameterisation of the prevertices.

We map the UHP to an isolated boulder polygonal region via the correspondence

$$\xi_1 = -1 \longleftrightarrow -\frac{b}{2} = z_1, \qquad \xi_2 = -\delta \longleftrightarrow -\frac{b}{2} + ic = z_2,$$
$$\xi_3 = \delta \longleftrightarrow \frac{b}{2} + ic = z_3, \qquad \xi_4 = 1 \longleftrightarrow \frac{b}{2} = z_4, \tag{4.1}$$

with exterior angles $\beta_1 = 1/2$, $\beta_2 = -1/2$, $\beta_3 = -1/2$ and $\beta_4 = 1/2$, respectively (Figure 10). The parameter δ is used to fix the lengths of the sides. The Schwarz–Christoffel map (2.6) is given by

$$z = f(\zeta) = A + \delta E_\delta \, \mathcal{E}\left(\zeta; \frac{1}{\delta}\right), \tag{4.2}$$

where $\mathcal{E}$ is the incomplete (Jacobi) elliptic integral of the second kind [3], and E_δ is a constant that scales with length [21, 73]. See Appendix D for details.

As discussed in the appendix, the conformal map in general cannot be specified exactly. In most cases, it must be solved numerically [69]. Nevertheless, we can make analytical progress. We choose to proceed with the parameterised mapping as in (4.2) because it has a simpler form. As for the step case, the most relevant quantity going forward is not the mapping $z = f(\zeta)$ itself, but its derivative given by

$$\frac{\mathrm{d}z}{\mathrm{d}\zeta} = f'(\zeta) = \sqrt{\frac{\zeta^2 - \delta^2}{\zeta^2 - 1}} \tag{4.3}$$

and the scaling constant E_δ. For illustration purposes, we will take $\delta = 1/2$.

The complex potential in conformal space for an isolated boulder (Appendix D) is given by

$$\omega = U_\infty E_\delta \zeta, \tag{4.4}$$

with velocity components (2.3)

$$u - iv = \frac{\mathrm{d}w}{\mathrm{d}z} = \frac{\mathrm{d}\omega}{\mathrm{d}\zeta} \Big/ \frac{\mathrm{d}z}{\mathrm{d}\zeta} = U_\infty \sqrt{\frac{\zeta^2 - 1}{\zeta^2 - \delta^2}}. \tag{4.5}$$

Again the velocity around an expansion corner ($>\pi$ rad) corner ($\zeta = \pm\delta$) is infinite, and zero at a $\pi/2$ rad corner ($\zeta = \pm 1$). Analogously, with the mapping (4.2) and velocity (4.5), we compute the flow speed (2.8) at any point around the isolated boulder. This is illustrated in Figure 11 with $\delta = 1/2$. The real values of ζ correspond to the solid boundary; specifically $\zeta \in (-1, -\delta)$ the front AC-face, $\zeta \in (-\delta, \delta)$ the top AB-face and $\zeta \in (\delta, 1)$ the rear AC-face of the boulder

https://doi.org/10.1017/S0956792519000214 Published online by Cambridge University Press

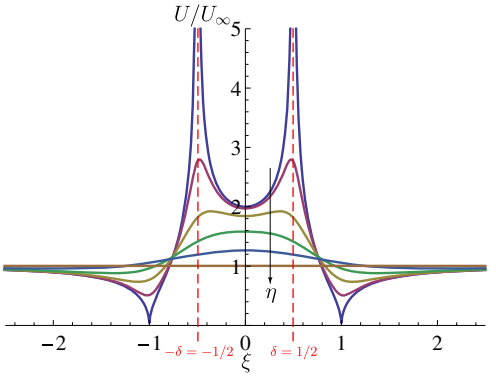


FIGURE 11. Flow speed U (2.8) and (4.5), normalised by background flow U_∞, in conformal space against ξ for $\eta = \{0, 0.1, 0.25, 0.5, 1, 10\}$. The arrow indicates increasing values of η. Further away from the boulder, as $|\xi|$ increases, $U \to U_\infty$. Along the boulder surface ($\eta = 0$), the flow speed is zero at the $\pi/2$ rad corners ($\xi = \pm 1$) and infinite at the $-\pi/2$ rad corners ($\xi = \pm\delta$). The front AC-face is in the region $\xi \in (-1, -\delta)$, the AB-face is in the region $\xi \in (-1, 1)$ and the rear AC-face is in the region $\xi \in (\delta, 1)$ (Figure 10). Here, $\delta = 1/2$ for illustration purposes.

(Figure 10). Symmetry implies that the velocity U on the front and rear faces is of the same magnitude.

Without specifying the mapping constants, we can make a few general remarks about the flow. As $|\xi|$ increases, $U \to U_\infty$, as expected. There exists a line of symmetry in the flow speed U about $\xi = 0$ ($= x$), while the velocity is unidirectional as $|x|$ and $|\xi| \to \infty$. Flow speed is increased ($U > U_\infty$) in the region above the AB-face, $|\xi| < \delta$ or $|x| < b/2$, with a minimum value $2U_\infty$.

4.3 Forces and moments

As with the step, the forces on the front AC ($\xi \in (-1, -\delta)$, $\eta = 0$), AB ($\xi \in (-\delta, \delta)$, $\eta = 0$) and rear AC ($\xi \in (\delta, 1)$, $\eta = 0$) faces of the boulder are non-trivial, due to the form of the flow (4.5). We combine both AC face contributions for the net force. Substituting the mapping (4.2) and flow (4.5) into the expression for the forces (2.15) gives

$$F_d^{\mathrm{AC_{front}}} - i F_l^{\mathrm{AC_{front}}} = -\frac{1}{2} i\rho a E_\delta U_\infty^2 \int_{-1}^{-\delta} \sqrt{\frac{\zeta^2 - 1}{\zeta^2 - \delta^2}}\, \mathrm{d}\zeta,$$
$$= -\frac{1}{2} i\rho a E_\delta U_\infty^2 \left[\mathcal{E}\left(1; \delta\right) - \mathcal{E}\left(1/\delta; \delta\right)\right], \tag{4.6a}$$

$$F_d^{\mathrm{AC_{rear}}} - i F_l^{\mathrm{AC_{rear}}} = -\frac{1}{2} i\rho a E_\delta U_\infty^2 \int_{\delta}^{1} \sqrt{\frac{\zeta^2 - 1}{\zeta^2 - \delta^2}}\, \mathrm{d}\zeta,$$
$$= -\frac{1}{2} i\rho a E_\delta U_\infty^2 \left[\mathcal{E}\left(1; \delta\right) - \mathcal{E}\left(1/\delta; \delta\right)\right], \tag{4.6b}$$

$$F_d^{\mathrm{AB}} - i F_l^{\mathrm{AB}} = -\frac{1}{2} i\rho a E_\delta U_\infty^2 \int_{-\delta}^{\delta} \sqrt{\frac{\zeta^2 - 1}{\zeta^2 - \delta^2}}\, \mathrm{d}\zeta,$$
$$= -\frac{1}{2} i\rho a 2 E_\delta U_\infty^2\, \mathcal{E}\left(1; \delta\right). \tag{4.6c}$$

https://doi.org/10.1017/S0956792519000214 Published online by Cambridge University Press

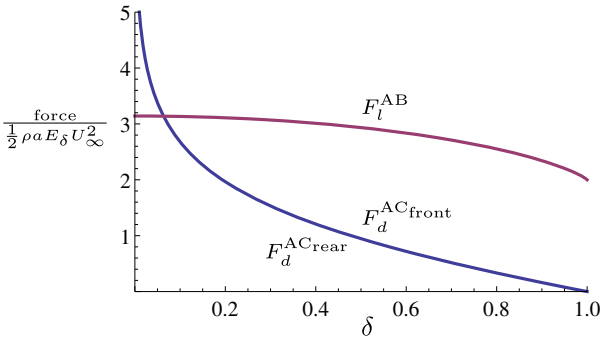


FIGURE 12. Drag and lift forces, F_d and F_l (4.6), on the AC and AB faces against δ, scaled with $\frac{1}{2}\rho a E_\delta U_\infty^2$. The drag forces are equal but act on opposite faces (D'Alembert's paradox), and the AB lift force is positive.

The elliptic function contributions on each AC face (4.6a,b) are purely imaginary, but equal. As they act on opposite sides, the net drag force is zero

$$F_d = F_d^{\mathrm{AC_{front}}} - F_d^{\mathrm{AC_{rear}}} = 0, \tag{4.7}$$

as expected from D'Alembert's paradox [29]. There is no drag force on the obstacle. On the AB face (4.6b), the quantity $\mathcal{E}\,(1;\delta)$ is real and positive for $\delta \in (0, 1)$. Hence, there is a lift force but no drag force. Note again that E_δ and δ are used to fix the width and height of the boulder. We expect the lift term to scale with the axis width b.

The forces, as they depend on δ, are shown in Figure 12. The lift force and each face of the drag force monotonically decrease with δ (as the obstacle gets wider and/or thinner). The drag force is zero for $\delta = 1$, which physically corresponds to a flat boundary ($c = 0$) (Figure 10). The lift force is always non-zero, even as $\delta \to 0$. Physically, this corresponds to flow over a slit domain ($b = 0$, $c > 0$) (Figure 10), so we expect the lift force to be zero.

We compare the hydrodynamic forces (4.6) with expressions in the literature (2.9), with the following correspondence:

$$F_d = \frac{1}{2}\,\rho\, C_d\, ac\, V^2 \longleftrightarrow 0, \tag{4.8a}$$

$$F_l = \frac{1}{2}\,\rho\, C_l\, ab\, V^2 \longleftrightarrow \frac{1}{2}\rho a 2 E_\delta\, \mathcal{E}\,(1;\delta)\, U_\infty^2. \tag{4.8b}$$

The lift coefficient is related by $C_l\, b\, V^2 \equiv 2E_\delta\, \mathcal{E}\,(1;\delta)\, U_\infty^2$. However, the drag coefficient clearly cannot be determined from this flow type. This and the non-zero lift force for $\delta \to 0$, as discussed (Figure 12), also cast doubt on the validity of the lift force calculation.

5 Separation and recirculation

The net drag force (4.7) by an inviscid flow on the isolated boulder is zero. This is an example of D'Alembert's paradox for potential flow (Section 2.5). To overcome the paradox, we consider a wake behind the boulder [43]. We impose a separated recirculation region as in Figure 13.

We model this situation by imposing doublet and vortex solutions behind the boulder. A parameterisation of their centres can be used to control the strength of the flow. The flow at the

https://doi.org/10.1017/S0956792519000214 Published online by Cambridge University Press

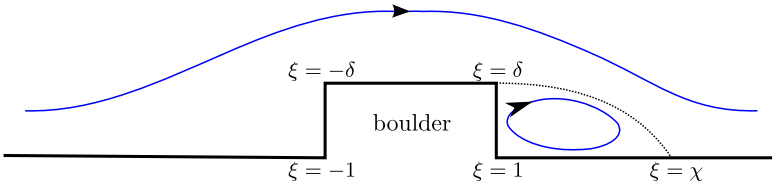


FIGURE 13. Schematic of the flow over an isolated boulder with a separated recirculation region behind the boulder. The solid lines are the rigid surfaces over which the fluid flows (arrows). The dashed line marks the boundary of the separation region (E1). The points of interest on the boundary are given by their conformal variable $\zeta = \xi + i\eta$ positions.

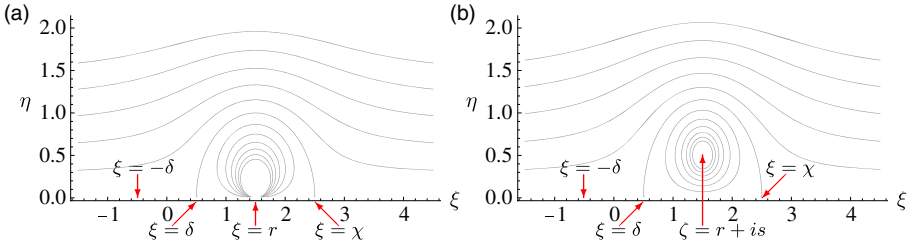


FIGURE 14. Streamlines (constant Ψ) of separated recirculation regions in conformal space (cf. Figure 13 for points in physical space). The separation occurs at the $\xi = \delta$ corner and reattaches behind the obstacle. (a) A doublet solution (5.1) occurs around $\xi = r$. (b) A vortex pair solution (5.6) occurs around $\xi = r + is$. Here, $\delta = 1/2, r = 3/2$ and $s = 1/2$ for illustration.

centre of a doublet or vortex is an unphysical singularity. However, it is the flow at the boundary of the recirculating regions that is physically relevant, and of interest here.

Using complex variables, we can generate these types of flow using only the flow direction along the boundary [74]. The complex potential is determined using the Generalised Poisson Integral. The details are given in Appendix E, based on Verhoff [73].

5.1 Doublet

The complex potential for a separated recirculation region based on a doublet at $\xi = r$ reads

$$\omega = \Phi + i\Psi = U_\infty E_\delta \left[\zeta - r + \frac{(\delta - r)^2}{\zeta - r}\right]. \tag{5.1}$$

See Appendix E for details. There is a singularity at $\xi = r$ on the boundary, but not on the obstacle's boundary for $r > 1$. We illustrate the streamlines (constant Ψ) in Figure 14 (a). Here, a separated recirculating region represented by a doublet (5.1) with $r = 3/2$ is shown. Varying the doublet centre r provides a tuning parameter to analyse forces for different flows.

We calculate the forces (2.15) on each face using the mapping (4.2) and complex potential (5.1),

$$F_d^{\mathrm{AC_{front}}} - i\,F_l^{\mathrm{AC_{front}}} = -\frac{1}{2} ia\rho E_\delta U_\infty^2 \int_{-1}^{-\delta} q_1(\zeta; r, \delta)\,\mathrm{d}\zeta\,, \tag{5.2a}$$

https://doi.org/10.1017/S0956792519000214 Published online by Cambridge University Press

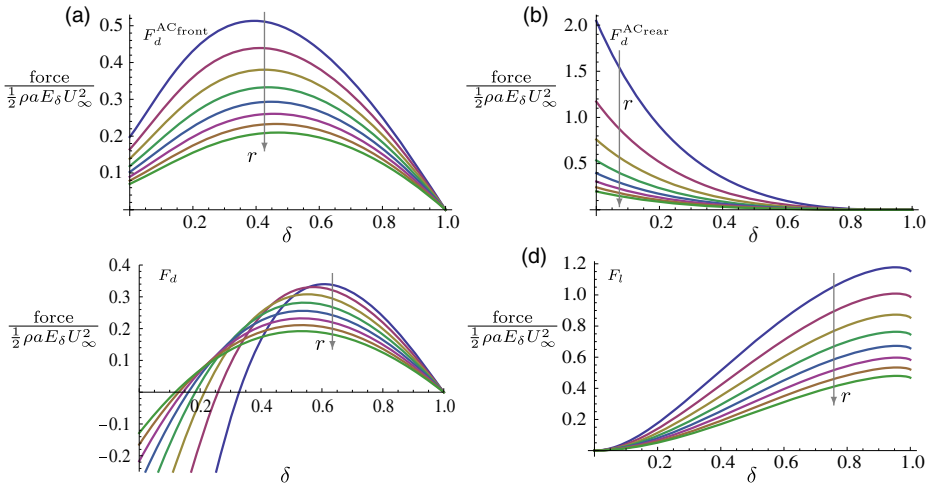


FIGURE 15. Forces on the obstacle against δ for different doublet positions r. The forces are scaled with $\frac{1}{2}a\rho E_\delta U_\infty^2$. (a) Drag on the front face (5.2a). (b) Drag on the rear face (5.2b). (c) Net drag (5.2a,b). (d) Lift on the top face (5.2c). The arrows point in the direction of increasing r, with curves taking values $r \in \{1.75, 2, 2.25, 2.5, 2.75, 3, 3.25, 3.5\}$.

$$F_d^{\mathrm{AC_{rear}}} - i\,F_l^{\mathrm{AC_{rear}}} = -\frac{1}{2} ia\rho E_\delta U_\infty^2 \int_\delta^1 q_1(\zeta; r, \delta)\,\mathrm{d}\zeta, \tag{5.2b}$$

$$F_d^{\mathrm{AB}} - i\,F_l^{\mathrm{AB}} = -\frac{1}{2} ia\rho E_\delta U_\infty^2 \int_{-\delta}^{\delta} q_1(\zeta; r, \delta)\,\mathrm{d}\zeta, \tag{5.2c}$$

where

$$q_1(\zeta; r, \delta) = \left(1 - \left(\frac{\delta - r}{\zeta - r}\right)^2\right)^2 \sqrt{\frac{\zeta^2 - 1}{\zeta^2 - \delta^2}}. \tag{5.3}$$

The drag on the AB face is zero ($F_d^{\mathrm{AB}} = 0$) and the lift force on the AC faces is zero ($F_l^{\mathrm{AC}} = 0$). Hence, the net drag on the boulder is that on the AC faces

$$\begin{aligned} F_d^{\mathrm{AC}} &= F_d^{\mathrm{AC_{front}}} - F_d^{\mathrm{AC_{rear}}} \\ &= \mathrm{Re}\left\{-\frac{1}{2} ia\rho E_\delta U_\infty^2 \left[\int_{-1}^{-\delta} q_1(\zeta; r, \delta)\,\mathrm{d}\zeta - \int_\delta^1 q_1(\zeta; r, \delta)\,\mathrm{d}\zeta\right]\right\}. \end{aligned} \tag{5.4}$$

With a wake, this is generally non-zero and D'Alembert's paradox is resolved. The hydrodynamic forces acting on the obstacle are shown in Figure 15. The forces are scaled with $\frac{1}{2}a\rho E_\delta U_\infty^2$ as E_δ must be calculated for each individual boulder geometry. The drag force goes to zero for $\delta \to 1$ and the lift force goes to zero as $\delta \to 0$, unlike the previous case (Figure 12). The drag on the rear AC-face increases significantly for obstacles with smaller δ. There is an optimal value of δ, a mapping parameter that increases with aspect ratio b/c, that maximises the drag force (Figure 16) for each doublet position r. This optimal value increases with r for the drag on the front AC face (Figure 16 (a)), but decreases for the overall drag (5.4) (Figure 16 (b)). As r increases, the optimal value of δ tends to a constant $\delta_{\max} \approx 0.53$.

https://doi.org/10.1017/S0956792519000214 Published online by Cambridge University Press

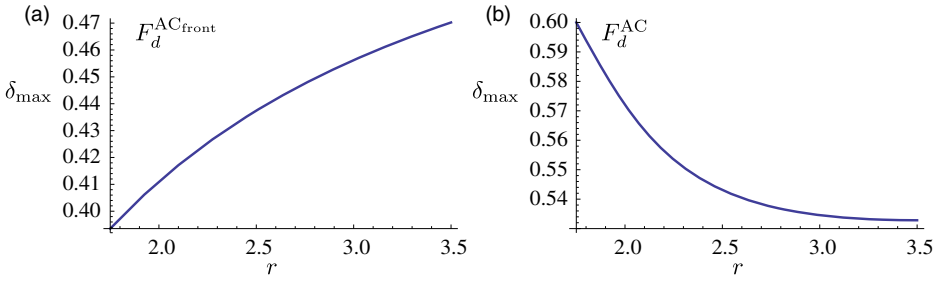


FIGURE 16. Geometric mapping parameter δ that maximises (a) drag force on the front AC face (5.2a) and (b) the overall drag force (5.4).

As the centre of the doublet moves away from the obstacle (r increases), the forces decrease. When r is close to the obstacle, with δ small, the net drag can be negative. This means that the separated recirculating region exerts a greater force than the background flow. The boulder would move against the flow if the hydrodynamic forces exceed the restraining forces.

The moment of the force (2.16) in a doublet flow is given by

$$M = \mathrm{Re}\left\{\frac{1}{2}\rho a E_\delta U_\infty^2 \int_{-1}^{1}\left[A + \delta E_\delta\, \mathcal{E}\left(\zeta;\frac{1}{\delta}\right)\right] q_1(\zeta; r, \delta)\,\mathrm{d}\zeta\right\}, \tag{5.5}$$

using (4.2), (5.1 and (5.3). In this form, there are too many unknown and variable parameters to calculate the moment, even for illustrative purposes. We present the expression (5.5) for completeness.

5.2 Vortex pair

The doublet solution (E5) provides a set of flows based on the parameter r along the boundary of the domain. We can model another set of separated flows by a vortex pair, using two parameters r and s for the location within the fluid. A separated recirculation region based on a vortex pair at $\zeta = r \pm is$ has complex potential

$$\omega = \Phi + i\Psi = U_\infty E_\delta\left[\zeta - r - i\frac{(\delta - r)^2 + s^2}{2s}\log\left(\frac{\zeta - r + is}{\zeta - r - is}\right)\right]. \tag{5.6}$$

The first term represents the uniform background flow and the log term the flow due to two vortices [4, 73]. This moves the singularity off the boundary, into the fluid. An illustration of the streamlines with separated recirculating regions represented by a vortex pair (5.6) with $r = 3/2$ and $s = 1/2$ is shown in Figure 14 (b).

Again using the mapping (4.2) and complex potential (5.6), we compute the forces (2.15) on each face,

$$F_d^{\mathrm{AC_{front}}} - i\,F_l^{\mathrm{AC_{front}}} = -\frac{1}{2}ia\rho E_\delta U_\infty^2 \int_{-1}^{-\delta} q_2(\zeta; r, s, \delta)\,\mathrm{d}\zeta, \tag{5.7a}$$

https://doi.org/10.1017/S0956792519000214 Published online by Cambridge University Press

$$F_d^{\mathrm{AC_{rear}}} - i\,F_l^{\mathrm{AC_{rear}}} = -\frac{1}{2} ia\rho E_\delta U_\infty^2 \int_\delta^1 q_2(\zeta; r, s, \delta)\,\mathrm{d}\zeta, \tag{5.7b}$$

$$F_d^{\mathrm{AB}} - i\,F_l^{\mathrm{AB}} = -\frac{1}{2} ia\rho E_\delta U_\infty^2 \int_{-\delta}^{\delta} q_2(\zeta; r, s, \delta)\,\mathrm{d}\zeta, \tag{5.7c}$$

where

$$q_2(\zeta; r, s, \delta) = \left(\frac{(\zeta - \delta)\,(\zeta + \delta - 2r)}{(r-\zeta)^2 + s^2} \right)^2 \sqrt{\frac{\zeta^2 - 1}{\zeta^2 - \delta^2}}. \tag{5.8}$$

The hydrodynamic forces are qualitatively similar to that of the doublet solution, with the forces diminishing as the centre of the vortex moves away from the boundary (Figure 17). Again, the drag force goes to zero for $\delta \to 1$ and the lift force goes to zero as $\delta \to 0$.

As with the doublet flow, the drag on the AB face is zero ($F_d^{\mathrm{AB}} = 0$) and the lift force on the AC faces is zero ($F_l^{\mathrm{AC}} = 0$). The net drag on the boulder is that on the AC faces

$$\begin{aligned} F_d^{\mathrm{AC}} &= F_d^{\mathrm{AC_{front}}} - F_d^{\mathrm{AC_{rear}}} \\ &= \mathrm{Re}\left\{ -\frac{1}{2} ia\rho E_\delta U_\infty^2 \left[\int_{-1}^{-\delta} q_2(\zeta; r, s, \delta)\,\mathrm{d}\zeta - \int_\delta^1 q_2(\zeta; r, s, \delta)\,\mathrm{d}\zeta \right] \right\}. \end{aligned} \tag{5.9}$$

Again, with a wake, this is generally non-zero and D'Alembert's paradox is resolved. An optimal value for the mapping parameter δ again maximises the drag force (Figure 18) for each vortex centre position $r + i\,s$. The optimal value for the front AC-face along increases with both r and s (Figure 18 (a)), but the overall drag (5.4) (Figure 18 (b)) is more complicated. As r increases, the optimal value of δ tends to a constant $\delta_{\max} \approx 0.53$, the same value as for the doublet, but for all s values. The optimal value $\delta_{\max}$ decreases with r for $s \lessapprox 0.75$ and increases with r for $s \gtrapprox 0.75$.

The moment of the force (2.16) in a vortex flow is given by

$$M = \mathrm{Re}\left\{ \frac{1}{2} \rho a E_\delta U_\infty^2 \int_{-1}^{1} \left[A + \delta E_\delta\, \mathcal{E}\left(\zeta; \frac{1}{\delta}\right) \right] q_2(\zeta; r, s, \delta)\,\mathrm{d}\zeta \right\}, \tag{5.10}$$

using (4.2), (5.6) and (5.8). Again, we present the expression (5.10) this for completeness.

5.3 Initiation of motion

Initiation of motion for an isolated boulder case is more complicated than a step-up, as in Section 3.4. A wake in the form of a separated recirculating region is imposed to overcome D'Alembert's paradox. The drag (5.2a,b; 5.7a,b) and lift (5.2c; 5.7c) forces are maximised for different boulder shapes, characterised by δ (Figures 16 and 18). However, the largest lift forces are significantly greater than the largest net drag forces. In the region of largest net drag, the lift force is still greater. This lift force may significantly reduce the restraining force (2.11b) for drag to overcome friction, resulting in motion (2.13a).

https://doi.org/10.1017/S0956792519000214 Published online by Cambridge University Press

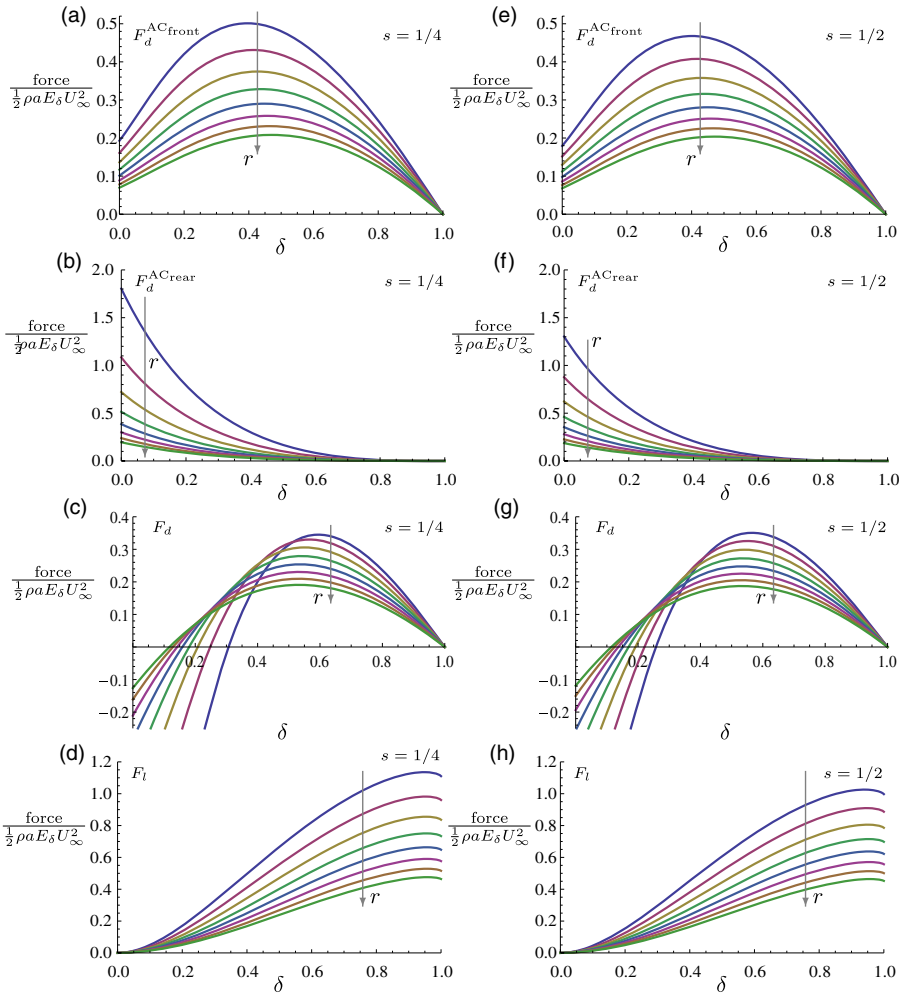


FIGURE 17. Forces on the obstacle against δ for different vortex pair positions $r + is$. The arrows point in the direction of increasing r, with curves taking values $r \in \{1.75, 2, 2.25, 2.5, 2.75, 3, 3.25, 3.5\}$. The left column takes $s = 1/4$, and the right column $s = 1/2$. The forces are scaled with $\frac{1}{2}a\rho E_\delta U_\infty^2$. (a,e) Drag on the front face (5.7a). (b,f) Drag on the rear face (5.7b). (c,g) Net drag (5.7a,b). (d,h) Lift on the top face (5.7c).

Similar to the joint-bound boulder, we determine the drag and lift coefficients that now depend only on geometry

$$\tilde{C}_d = \frac{1}{c}\,\mathrm{Re}\left\{iE_\delta\left[\left(\int_\delta^1 - \int_{-1}^{-\delta}\right)Q(\zeta)\,\mathrm{d}\zeta\right]\right\}, \tag{5.11a}$$

$$\tilde{C}_l = \frac{1}{b}\,\mathrm{Re}\left\{E_\delta\int_{-\delta}^{\delta}Q(\zeta)\,\mathrm{d}\zeta\right\}, \tag{5.11b}$$

where in each case $Q(\zeta) = q_1(\zeta; r, \delta)$ for the doublet flow and $Q(\zeta) = q_2(\zeta; r, s, \delta)$ for the vortex pair flow.

https://doi.org/10.1017/S0956792519000214 Published online by Cambridge University Press

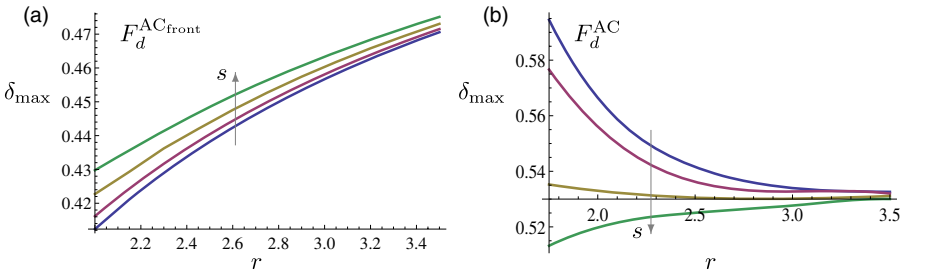


FIGURE 18. Geometric mapping parameter δ that maximises (a) drag force on the front AC face (5.7a) (b) the overall drag force (5.9). The centre of the vortex is positioned at $\zeta = r + is$ in conformal space, with the curves plotted against r for $s = \{0.25, 0.5, 0.75, 1\}$. The arrow points in the direction of increasing s.

Substituting and rearranging the forces (5.4) and (5.9) and moments (5.5) and (5.10), we solve for the predicted velocity required to initiate motion (2.13, in terms of the mapping parameters,

$$U_\infty^2 > 2\mu \frac{\rho_s - \rho}{\rho} gbc \left(\mathrm{Re}\left\{ iE_\delta \left[\left(\int_\delta^1 - \int_{-1}^{-\delta} \right) Q(\zeta)\,\mathrm{d}\zeta \right] \right\} + \mu \mathrm{Re}\left\{ E_\delta \int_{-\delta}^{\delta} Q(\zeta)\,\mathrm{d}\zeta \right\} \right)^{-1} \quad \text{(nudging)}, \tag{5.12a}$$

$$U_\infty^2 > \mu \frac{\rho_s - \rho}{\rho} gb^2 c \left(\mathrm{Re}\left\{ E_\delta \int_{-1}^{1} \left[A + \delta E_\delta\, \mathcal{E}\left(\zeta; \frac{1}{\delta}\right) \right] Q(\zeta)\,\mathrm{d}\zeta \right\} \right)^{-1} \quad \text{(overturning)}, \tag{5.12b}$$

$$U_\infty^2 > 2\mu \frac{\rho_s - \rho}{\rho} gbc \left(\mathrm{Re}\left\{ E_\delta \int_{-\delta}^{\delta} Q(\zeta)\,\mathrm{d}\zeta \right\} \right)^{-1} \quad \text{(lift)}, \tag{5.12c}$$

again with $Q(\zeta) = q_1(\zeta; r, \delta)$ for the doublet flow and $Q(\zeta) = q_2(\zeta; r, s, \delta)$ for the vortex pair flow.

The strength of the doublet or vortex pair on the obstacle, given by its position, has a significant effect on the net drag force. In particular, when the obstacle is thin and/or tall, for example, c/b is large or δ is small, the drag force on the rear face is greater than the front face (Figures 15 (c) and 17 (c,g)). In this case, any sliding motion will be against the flow. The range of δ resulting in this motion decreases as the centre of the recirculating region moves away from the obstacle.

We may parameterise the flow for a doublet and vortex pair, with r and $r + is$, respectively. For *a priori* knowledge of the wake, matching the above parameters for a representation of the flow can allow computation of the hydrodynamic forces and indicate initiation of motion.

6 Conclusions

We model potential flow around two representative submerged boulder situations, a joint-bound boulder and an isolated boulder (Figure 2). We use conformal mapping (Schwarz–Christoffel) techniques to transform the problem to the UHP. We solve the flow problem in conformal space and map the solution back to physical space. The resulting flows are non-trivial. The mappings result in stagnant flows at $\pi/2$ rad corners and singularities at expansion $3\pi/2$ rad corners

https://doi.org/10.1017/S0956792519000214 Published online by Cambridge University Press

(Figures 4 and 11). We retain the singular profile as it is local and integrable. However, potential flow around a rectangular protrusion (isolated boulder) exhibits further non-physical aspects, such as D'Alembert's paradox. The singularities are removed from the boundary, and the paradox resolved, by imposing a wake behind the obstacle.

In all cases, drag forces are only exerted on faces normal to the flow and lift forces on faces parallel to the flow, as expected. However, the magnitudes of these forces are different to values found in the literature. A depth-averaged flow assumes that the flow is the same on all faces of the boulder. However, we show that this is not the case. The far-field velocity U_∞ takes the place of a depth-averaged velocity V, with the geometry dictating local effects in the flow around the boulder.

For the step-up, the drag force (3.6a) takes a similar form to the literature (3.8a) if the drag coefficient is $\tilde{C}_d = 1$ (3.9a). The lift force (3.6b) has a non-linear dependence on the aspect ratio of the boulder (Figure 5). The corresponding lift coefficient (3.9b) is also significantly larger than appears in the literature (Figure 6 (a)), with a range $\tilde{C}_l = 1.5$–3 for typical aspect ratios b/c. This corresponds with hypothesised values in the literature [57]. The drag moment (3.10a) has a similar variable and geometry dependence as in the literature (3.12a), but is a factor of ≈ 1.81 greater. The lift moment (3.10a) depends on the geometry, increasing with aspect ratio b/c. However it is less than the value in the literature (Figure 6 (b)).

Initiation of motion is modelled by force and moment balances (2.13) dictating the type of motion. For a joint-bound boulder (Section 3), sliding is not possible. The geometry determines whether overturning or lift is first initiated, that is, requiring a smaller flow velocity U_∞. The switch over point is $b/c = 1.793$ (Figure 7). Our predicted velocities (Figure 8) required for initiation of motion are significantly reduced compared to the models in the literature (Figure 9). For boulders $b, c = 1$–$2\,\mathrm{m}$, motion is induced with velocities $U_\infty = 3$–$4\,\mathrm{m/s}$ (Table 1). The larger lift forces in our model help to understand boulder movement against gravity as observed in the field [20].

Laminar potential flow over an isolated (stand-alone) boulder immediately encounters D'Alembert's paradox. The net drag force (4.6a,b) is zero. Furthermore, the lift force (4.6c) is non-zero for $\delta \to 0$ (Figure 12). A wake is imposed behind the boulder, for physicality (Figure 14). We impose the form of a separated recirculating region based on doublets and vortex pairs. The drag and lift forces are qualitatively similar (Figures 15 and 17). The forces decrease as the doublet and vortex pair positions move away from the obstacle. This is more significant on the rear face than the front face. The drag is maximised for a non-trivial geometry (based on mapping parameter δ that increases with aspect ratio b/c). This optimal value tends to a constant $\delta_{\max} \approx 0.53$ for both the doublet and vortex pair flows as their centres move downstream (Figures 16 (b) and 18 (b)). We present closed-form expressions of the hydrodynamic coefficients (5.11) that depend only on geometry.

For an isolated boulder on a flat platform, a wake allows a net drag to initiate sliding. Typically, the lift force is greater than the net drag (Figures 15 (c,d) and 17 (c,g,d,h)). Here, the friction force (2.11b) is reduced by a lift buoyancy. In this situation, the boulder may be subject to sliding, overturning and lift. Thinner and taller boulders (smaller δ) may be transported against the flow ($F_d < 0$ as in Figures 15 (c) and 17 (c,g)). Although theoretically possible, with observations in the field (though usually attributed to return flows [36]), it is more likely only physically realisable in more constrained geometries with high pressure in the wake. We provide the velocity conditions (5.12) to initiate each type of motion.

https://doi.org/10.1017/S0956792519000214 Published online by Cambridge University Press

7 Discussion

7.1 Context of the model

Flow over a rectangular obstacle is non-trivial. The model assumes that the obstacle is stationary. In theory, the model applies in the reference frame where the (isolated) obstacle is moving at a constant relative velocity to the fluid flow. However, transport of large obstacles such as boulders with constant velocity (i.e. no acceleration) is unlikely. We apply our models to situations of subtidal/fully submerged boulders such as during tsunami inundations, strong storm surges and strong tidal currents.

Throughout the analysis, we find that geometry almost fully determines the system. The velocity predictions are given in terms of a uniform background flow. Near the boulder, the local effects depend only on geometry, specifically the aspect ratio b/c for the joint-bound case or δ for the isolated case. In particular, for the joint-bound case we determine drag and lift coefficients (3.8) that emerge from our calculations. It is well known that the experiments for determining C_l do not represent a real-field situation. The lift coefficient $\tilde{C}_l$ (Figure 6) we calculate is an order of magnitude greater than the $C_l = 0.178$ in the literature (cf. Section 2.6), fitting with other predictions based on necessary values to fit observed boulder movements [57]. We present closed-form expressions of the hydrodynamic coefficients (5.11) for the isolated boulder case.

The non-linear flow around the boulder enhances the hydrodynamics, reducing the predicted velocities for motion by more than 1/2 (Figure 9). This has implications for debate on the cause of boulder movement, storms or tsunamis. Models in the literature predicted storm velocities that were much too large for storm inundations, but the field evidence clearly shows movement by storms. Our model suggests velocities in the 3–4 m/s range (Table 1) that can be better associated with storms.

The isolated boulder is modelled with either a doublet or vortex pair. These flows have singularities at their centres. However, as stated in the text, it is the flow at the boundary of the recirculating regions that is physically relevant. We envisage an application of our model where the recirculating region is matched to observed conditions. Then the hydrodynamics may be determined from our model.

Finally, our model is applicable to any situation of an obstacle submerged in a constant flow, such as underwater structures in marine and civil engineering.

7.2 Mathematical technicalities

The Schwarz–Christoffel mapping (2.6) allows us to solve for the flow in a simple geometric setting, and to map the solution back to physical space around the obstacle. The mapping to the isolated boulder (4.2) is limited by our knowledge of the constants. As discussed, the prevertices $\pm\delta$ are problem specific and, along with the constants, are often determined numerically [69]. We consider a symmetric set of prevertices because the polygon is rectangular [15]. We must also consider the branch points, and choices of branch cuts, that arise from square root and logarithm functions of complex variables. It is important to note that these choices are known to be inconsistent among different software packages.

A drawback of the conformal mapping method is that it introduces singularities when corners are greater than π rad. However, these singularities are local features. The model can be

https://doi.org/10.1017/S0956792519000214 Published online by Cambridge University Press

enhanced by introducing regularisation methods at such corners, such as viscosity [23, 34, 47], or smoothing the corner. The introduction of a free surface would make the model more realistic. Waves passing over obstacles are affected by their presence (see Introduction), which in turn affects the localised flow around the object in both time and space [70]. However, we may neglect contributions from free-surface interactions by assuming either small wave events such as tidal currents, or small obstacle height to fluid depth.

We use Blasius' theorem to determine the forces on the obstacles [4]. Alternative methods for calculating force include a direct integration of the pressure around the obstacle [33] and an integration of the product of the complex velocity and its conjugate [29]. We choose the method of Blasius' theorem because of the simple form of the integrand.

We consider a separated recirculating layer emanating from the rear top corner (Section 5). We generate this flow as opposed to solving for it, and it simply moves the singularity away from the obstacle's boundary [73] (which is better than on the boundary). However, it serves many purposes. Firstly, similar recirculating regions are physically observed to those discussed in [62, 64, 65]. Secondly, it overcomes D'Alembert's paradox [43]. Thirdly, it introduces parameters to generalise the flow, so that it may provide a reference for an observed flow. The positions of the doublet ($\zeta = r$) and vortex pair ($\zeta = r + is$), along with the obstacle shape (δ), determine the size of the separated region and the force distribution on the obstacle. For instance, we expect r to increase with Reynolds number.

The net drag force can be greater on the rear face than the front face (Figures 15 (c) and 17 (c,g)), meaning that any movement will be against the flow. Although counter-intuitive, this type of movement is observed but mostly attributed to returning flows [36]. There may, however, be situations controlled by geometry where the pressure is enhanced on the rear side.

We consider a separated circulating region only for an isolated boulder. Although physically observed for the step-up with a turbulent boundary layer [62], our analytical method in Section 5.1 only allows for detachment and reattachment at the same point. This situation is too unphysical to pursue. Furthermore, the boulders are 3D objects, whereas the models presented are 2D. Despite the wake around a cube being most pronounced behind the cube [41], the edge effects may still contribute significantly to the hydrodynamic forces. This is highlighted by the unstable nature of doublets and vortices in 3D [63].

Appendix A Notation

A list of important and commonly used notation, with a description, is given in Table A1.

Appendix B Hydrodynamic forces

The forces from a steady potential flow can be computed directly from the complex potential. Blasius's theorem relates the net horizontal (F_x) and vertical (F_y) forces to an integral around a closed curve, C, of the boundary [4],

$$F_x - i F_y = \frac{1}{2} i\rho \oint_C \left(\frac{\mathrm{d}w}{\mathrm{d}z}\right)^2 \mathrm{d}z. \tag{B1}$$

The horizontal and vertical forces represent the drag and lift, $F_x = F_d$ and $F_y = F_l$, respectively [33]. In the case of an obstacle along the bottom surface to the flow, as in Figure 2, the

https://doi.org/10.1017/S0956792519000214 Published online by Cambridge University Press

Table A1. *Table of symbols, with brief description and units if relevant*

Symbol	Description	Units
a, b, c	Length, width, height of boulder	m
A, B, C	Boulder axes	
K	Bernoulli constant	$\mathrm{m^2\ s^{-2}}$
p	Pressure	$\mathrm{kg\ m^{-1}\ s^{-2}}$
g	Gravitational acceleration	$\mathrm{m\ s^{-2}}$
ρ, ρ_s	Density of water and rock	$\mathrm{kg\ m^{-3}}$
x, y	Physical space	m
$z = x + iy$	Physical plane	m
u, v	Horizontal and vertical velocities	$\mathrm{m\ s^{-1}}$
Φ, Ψ	Velocity potential and stream function	$\mathrm{m^2\ s^{-1}}$
$w = \Phi + i\Psi$	Complex potential	$\mathrm{m^2\ s^{-1}}$
f	Schwarz–Christoffel mapping function	
β	Exterior angle	rad
$\mathcal{E}$	Incomplete Jacobi Elliptic function (second kind)	
U	Flow speed	$\mathrm{m\ s^{-1}}$
U_∞	Far-field uniform velocity	$\mathrm{m\ s^{-1}}$
V	Depth-averaged velocity	$\mathrm{m\ s^{-1}}$
F_d, F_l	Drag and lift force	$\mathrm{kg\ m\ s^{-2}}$
F_m, F_f, F_g	Inertia, friction and gravitational force	$\mathrm{kg\ m\ s^{-2}}$
C_d, C_l, μ	Coefficient of drag, lift and friction	
M_d, M_l, M_m, M_g	Drag, lift, inertia and gravitational moment	$\mathrm{kg\ m^2\ s^{-2}}$
$\tilde{C}_d$	New drag coefficient (geometry-dependent)	
$\tilde{C}_l$	New lift coefficient (geometry-dependent)	
κ_M	Lift moment scaling factor	
Θ_F, Θ_M	Lift force and moment functions of position	
$\mathcal{R}$	Ratio of sliding to overturning criteria	
ξ, η	Conformal space	
$\zeta = \xi + i\eta$	Conformal plane	
ω	Conformal complex potential	
χ	Conformal reattachment point	
$r, r + is$	Doublet and vortex pair centre positions	
$q_1(\zeta; r, s)$	Integrand function for doublet	
$q_2(\zeta; r, s, \delta)$	Integrand function for vortex pair	
δ	Isolated boulder prevertex mapping point	
E_δ	Isolated boulder mapping scaling	

exposed surfaces do not form a closed curve. Following the derivation in Acheson [4], the forces on each boundary element are modified by a constant, K, arising from Bernoulli's principle,

$$\delta F_x - i\,\delta F_y = \frac{1}{2} i\rho \left(\frac{\mathrm{d}w}{\mathrm{d}z}\right)^2 \delta z - Ki(\delta x - i\delta y). \tag{B2}$$

The K term disappears when integrating around a closed curve, resulting in Eq. (B1). However, we have not yet specified a reference pressure for the system, which can be chosen such that K is zero [29]. Physically, we should account for all pressure in the system. The rectangular geometry of the obstacles (Figure 2) means that accommodating a non-zero K in an integral around the boundary is simple. To account for 3D effects, where the flow applies force to the

https://doi.org/10.1017/S0956792519000214 Published online by Cambridge University Press

face of a boulder, we factor in the length of the A-axis, a. Hence, the forces acting on an obstacle are given by

$$F_d - i\,F_l = aK\int \mathrm{d}y + iabK + \frac{1}{2}i\rho a\int_{C_e}\left(\frac{\mathrm{d}w}{\mathrm{d}z}\right)^2 \mathrm{d}z, \tag{B3}$$

where C_e is the exposed surface. Note that the integration is performed clockwise, and thus changes the sign on the Bernoulli terms [4]. For the joint-bound boulder case, $\int \mathrm{d}y = c$ (Figure 2 (a)). Interestingly, the Bernoulli term increases one force and decreases the other, depending on the sign of K. However for the isolated boulder case, $\int \mathrm{d}y = 0$ as the two sides cancel out (Figure 2 (b)). We will find it is easier to compute this integral in conformal space, with

$$\mathrm{d}z = \frac{\mathrm{d}z}{\mathrm{d}\zeta}\,\mathrm{d}\zeta, \tag{B4a}$$

$$\frac{\mathrm{d}w}{\mathrm{d}z} = \frac{\mathrm{d}\omega}{\mathrm{d}\zeta}\Big/\frac{\mathrm{d}z}{\mathrm{d}\zeta}, \tag{B4b}$$

via (2.6) and (2.7). For simplicity, take $K = 0$, and hence

$$F_d - i\,F_l = -\frac{1}{2}i\rho a\int_{C_\zeta}\left[\left(\frac{\mathrm{d}\omega}{\mathrm{d}\zeta}\right)^2\Big/\frac{\mathrm{d}z}{\mathrm{d}\zeta}\right]\mathrm{d}\zeta, \tag{B5}$$

where C_ζ is the exposed boundary in the ζ-plane. We integrate in the clockwise direction (increasing ζ) around the obstacle, and thus include an additional minus sign.

Appendix C Joint-bound boulder

We map the UHP to the stepped polygonal region via the correspondence

$$\xi_1 = -1 \longleftrightarrow 0 = z_1, \qquad \xi_2 = 1 \longleftrightarrow ic = z_2, \tag{C1}$$

where the exterior angles are $\beta_1 = 1/2$ and $\beta_2 = -1/2$, respectively (Figure 3). The Schwarz–Christoffel map (2.6) is given by

$$\begin{aligned} z = f(\zeta) &= A + B\int^{\zeta}\sqrt{\frac{t-1}{t+1}}\,\mathrm{d}t, \\ &= A + B\left(\sqrt{\zeta^2-1} - \cosh^{-1}(\zeta)\right). \end{aligned} \tag{C2}$$

Substituting $f(-1) = 0$ and $f(1) = ic$ gives the mapping [44]

$$z = x + iy = f(\zeta) = ic + \frac{c}{\pi}\left(\sqrt{\zeta^2-1} - \cosh^{-1}(\zeta)\right). \tag{C3}$$

Note that in the far field, $z \to c\,\zeta/\pi$.

We can easily solve for the complex potential in the UHP. In physical space, the complex potential w satisfies Laplace's equation with an impenetrable boundary along the step. The far-field condition (3.1) is uniform flow, that is, $w = U_\infty z$. In conformal space, the complex potential ω also satisfies Laplace's equation. Here, the real axis ($\eta = 0$) of the UHP

https://doi.org/10.1017/S0956792519000214 Published online by Cambridge University Press

represents the boundary $\partial f^{-1}(D)$, and the corresponding far-field condition is determined from the mapping (3.3), that is, $w \to U_\infty c\zeta/\pi$. The system is given by

$$\nabla^2 \omega = 0, \qquad \eta > 0, \tag{C4a}$$

$$\operatorname{Im} \omega = 0, \qquad \eta = 0, \tag{C4b}$$

$$\omega \sim \frac{U_\infty c\zeta}{\pi}, \qquad \zeta \to \infty, \tag{C4c}$$

with solution

$$\omega = \frac{U_\infty c\zeta}{\pi}. \tag{C5}$$

The velocity components (2.3) are

$$\begin{aligned} u - iv &= \frac{\mathrm{d}w}{\mathrm{d}z} = \frac{\mathrm{d}\omega}{\mathrm{d}\zeta} \Big/ \frac{\mathrm{d}z}{\mathrm{d}\zeta} \\ &= U_\infty \sqrt{\frac{\zeta + 1}{\zeta - 1}}. \end{aligned} \tag{C6}$$

Appendix D Isolated boulder

We map the UHP to an isolated boulder polygonal region via the correspondence

$$\xi_1 = -1 \longleftrightarrow -\frac{b}{2} = z_1, \qquad \xi_2 = -\delta \longleftrightarrow -\frac{b}{2} + ic = z_2,$$

$$\xi_3 = \delta \longleftrightarrow \frac{b}{2} + ic = z_3, \qquad \xi_4 = 1 \longleftrightarrow \frac{b}{2} = z_4, \tag{D1}$$

with exterior angles $\beta_1 = 1/2$, $\beta_2 = -1/2$, $\beta_3 = -1/2$ and $\beta_4 = 1/2$, respectively (Figure 10). The parameter δ is used to fix the lengths of the sides. The Schwarz–Christoffel map (2.6) is given by

$$\begin{aligned} z = f(\zeta) &= A + B \int^{\zeta} \sqrt{\frac{t^2 - \delta^2}{t^2 - 1}}\, \mathrm{d}t, \\ &= A + \delta E_\delta \, \mathcal{E}\left(\zeta; \frac{1}{\delta}\right), \end{aligned} \tag{D2}$$

where $\mathcal{E}$ is the incomplete (Jacobi) elliptic integral of the second kind [3], and E_δ is a constant that scales with length. Regarding notation, we define the elliptic integral in the Jacobi form, $\mathcal{E}(x; m) = \int_0^x \frac{\sqrt{1-m^2t^2}}{\sqrt{1-t^2}}\, \mathrm{d}t$. We note this as alternative definitions take the first input in trigonometric form and the second input as $k = m^2$. In the far field, $z \to E_\delta \zeta$.

Elliptic integrals such as (D2) typically appear in problems with mappings to a rectangle. However, the constants A and E_δ are non-trivial [21, 73]. The Schwarz–Christoffel mapping guarantees that angles are preserved, but it can be a challenge to prescribe lengths. One must solve for the appropriate prevertices, but this may not give an explicit result even when exploiting symmetry in the problem [15]. Here, we choose prevertices -1, $-\delta$, δ, 1 and ∞, and define

https://doi.org/10.1017/S0956792519000214 Published online by Cambridge University Press

the height of the boulder via the value of δ (Figure 10). The constant E_δ fixes the width [73]. However, determining δ and E_δ for a particular geometry may be elusive [21].

The complex potential in conformal space for an isolated boulder only differs from the joint-bound boulder by the far-field condition, that is, $w \to U_\infty E_\delta \zeta$. The system is given by

$$\nabla^2 \omega = 0, \qquad \eta > 0, \tag{D3a}$$

$$\operatorname{Im} \omega = 0, \qquad \eta = 0, \tag{D3b}$$

$$\omega \sim U_\infty E_\delta \zeta, \qquad \zeta \to \infty, \tag{D3c}$$

with solution

$$\omega = U_\infty E_\delta \zeta. \tag{D4}$$

The velocity components (2.3) are given by

$$\begin{aligned} u - iv &= \frac{\mathrm{d}w}{\mathrm{d}z} = \frac{\mathrm{d}\omega}{\mathrm{d}\zeta} \Big/ \frac{\mathrm{d}z}{\mathrm{d}\zeta} \\ &= U_\infty \sqrt{\frac{\zeta^2 - 1}{\zeta^2 - \delta^2}}. \end{aligned} \tag{D5}$$

Appendix E Separated recirculating doublet

We consider a separated recirculation region to overcome D'Alembert's paradox for the isolated boulder case (Section 2.5). Writing the velocity as $\mathrm{d}w/\mathrm{d}z = q \exp(-i\theta)$, we impose the flow direction $\theta = \theta_b$ along the boundary such that it flows towards the right except for the region $\xi \in (\delta, \chi)$, where it travels towards the left (Figure 13). This is represented by

$$\theta_b = \begin{cases} 0 & \xi < -1, \\ \frac{\pi}{2} & -1 < \xi < -\delta, \\ 0 & -\delta < \xi < \delta, \\ \frac{\pi}{2} & \delta < \xi < 1, \\ -\pi & 1 < \xi < \chi, \\ 0 & \chi < \xi. \end{cases} \tag{E1}$$

We must solve for the point χ such that the circulation region is closed [73].

The Generalised Poisson Integral formula generates an analytic function F on the UHP using the real-axis boundary values [74]. By considering the log of the velocity, we can isolate the boundary points using only the (imaginary) flow direction θ_b (E1) that is assumed *a priori*. The Generalised Poisson Integral formula, for the imaginary part of $\log(\mathrm{d}w/\mathrm{d}z)$ at the boundary ($= -\theta_b$), is given by

$$F(\zeta) = \frac{1}{\pi} \int_{-\infty}^{\infty} \frac{\theta_b}{\zeta - \sigma} \, \mathrm{d}\sigma, \tag{E2a}$$

$$= \frac{1}{2} \log(\zeta + 1) - \frac{1}{2} \log(\zeta + \delta) + \frac{1}{2} \log(\zeta - \delta) - \frac{3}{2} \log(\zeta - 1) + \log(\zeta - \chi). \tag{E2b}$$

https://doi.org/10.1017/S0956792519000214 Published online by Cambridge University Press

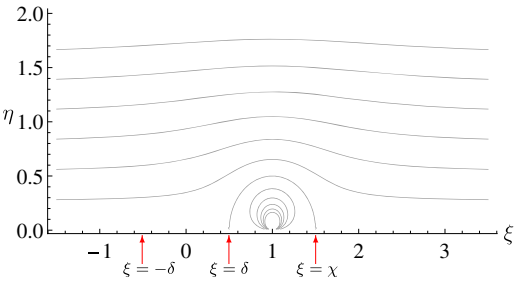


FIGURE E1. Streamlines, lines of constant Ψ (E5), of a separated recirculation region in conformal space (cf. Figure 13 for points in physical space). The separation occurs at the $\xi = \delta$ corner and reattaches behind the obstacle at $\xi = \chi = 2 - \delta$. A doublet-like solution occurs around $\xi = 1$. Here, $\delta = 1/2$ for illustration.

The velocity is determined by

$$\frac{\mathrm{d}w}{\mathrm{d}z} = U_\infty \exp(F) = U_\infty \frac{(\zeta+1)^{\frac{1}{2}}(\zeta-\delta)^{\frac{1}{2}}(\zeta-\chi)}{(\zeta+\delta)^{\frac{1}{2}}(\zeta-1)^{\frac{3}{2}}}, \tag{E3a}$$

$$\Rightarrow \frac{\mathrm{d}\omega}{\mathrm{d}\zeta} = U_\infty E_\delta \frac{(\zeta-\delta)(\zeta-\chi)}{(\zeta-1)^2}, \tag{E3b}$$

using (4.2). We note that there is no longer a singularity at the $-\pi/2$ rad corners ($\zeta = \pm\delta$). However, there is now a doublet-like solution at $\zeta = 1$ that arises using the Generalised Poisson Integral formula [73]. Integrating for the complex potential,

$$\omega = \Phi + i\Psi = U_\infty E_\delta \left[\zeta + \frac{-1+\chi+\delta-\chi\delta}{\zeta-1} - (-2+\chi+\delta)\log(\zeta-1)\right] + \text{const}, \tag{E4}$$

reveals that, to construct a closed separation region, we must impose $\chi = 2 - \delta$ to remove the log term that generates an arctangent in the streamfunction Ψ. Hence,

$$\omega = \Phi + i\Psi = U_\infty E_\delta \left[\zeta - 1 + \frac{(\delta-1)^2}{\zeta-1}\right]. \tag{E5}$$

We have fixed the constant such that the second term in brackets is -1, as $\zeta = 1$ is the centre of the doublet. The constant does not affect the flow. In the non-separation case (4.4), the conformal-space complex potential scales linearly with ζ. In the separating case (E5), the complex potential asymptotically scales linearly with ζ as $\zeta \to \infty$, but is non-linear near the obstacle. The streamlines, constant Ψ (E5), show the separated recirculating region (Figure E1). The separation occurs at the $\xi = \delta$ corner and reattaches behind the obstacle with the rear face ($\xi \in (\delta, 1)$, $\eta = 0$) exposed to the recirculating flow.

The doublet form of the velocity (E3b) results in a non-integrable singularity for the forces (2.15) at $\xi = 1$. However, this is just one construction of a recirculating region. Following the methods of Verhoff [73], we can generalise the separated recirculating region to be centred at any point, specifically one not on the boulder's boundary. Generalising the separated recirculation region (E5) to a doublet at $\xi = r$, the complex potential reads

$$\omega = \Phi + i\Psi = U_\infty E_\delta \left[\zeta - r + \frac{(\delta-r)^2}{\zeta-r}\right]. \tag{E6}$$

The singularity is still on the boundary, but not on the obstacle's boundary for $r > 1$.

https://doi.org/10.1017/S0956792519000214 Published online by Cambridge University Press

Acknowledgements

This study was funded by the Science Foundation Ireland (SFI) under the research project 'Understanding Extreme Nearshore Wave Events through Studies of Coastal Boulder Transport' (14/US/E3111).

References

[1] Abd-el Malek, M. B., Hanna, S. N. & Kamel, M. T. (1991) Approximate solution of gravity flow from a uniform channel over triangular bottom for large froude number. *Appl. Math. Model.* **15**(1), 25–32.

[2] Abd-el Malek, M. B. & Masoud, S. Z. (1988) Linearized solution of a flow over a ramp. *Appl. Math. Model.* **12**(4), 406–410.

[3] Abramowitz, M., Stegun, I. A., et al. (1972) *Handbook of Mathematical Functions with Formulas, Graphs, and Mathematical Tables*, vol. 9. Dover, New York.

[4] Acheson, D. J. (1990) *Elementary Fluid Dynamics*. Clarendon Press, Wotton-under-Edge.

[5] Akrish, G., Rabinovitch, O. & Agnon, Y. (2016) Extreme run-up events on a vertical wall due to nonlinear evolution of incident wave groups. *J. Fluid Mech.* **797**, 644–664.

[6] Akrish, G., Schwartz, R., Rabinovitch, O. & Agnon, Y. (2016) Impact of extreme waves on a vertical wall. *Nat. Hazards* **84**(2), 637–653.

[7] Alexander, J. & Cooker, M. J. (2016) Moving boulders in flash floods and estimating flow conditions using boulders in ancient deposits. *Sedimentology* **63**(6), 1582–1595.

[8] Balta, S. & Smith, F. T. (2018) Fluid flow lifting a body from a solid surface. *Proc. Roy. Soc. A*, 474(2219), 20180286.

[9] Batchelor, G. K. (1967) *An Introduction to Fluid Dynamics*. Cambridge University Press, Cambridge.

[10] Belward, S. R. & Forbes, L. K. (1993) Fully non-linear two-layer flow over arbitrary topography. *J. Eng. Math.* **27**(4), 419–432.

[11] Binder, B. J., Vanden-Broeck, J.-M. & Dias, F. (2005) Forced solitary waves and fronts past submerged obstacles. *Chaos: An Interdisciplinary J. Nonlinear Sci.*, **15**(3), 037106.

[12] Biolchi, S., Furlani, S., Antonioli, F., Baldassini, N., Deguara, J. C., Devoto, S., Di Stefano, A., Evans, J., Gambin, T., Gauci, R., et al. (2016) Boulder accumulations related to extreme wave events on the eastern coast of Malta. *Nat. Hazards Earth Syst. Sci.* **16**, 737–756.

[13] Bot, P., Rabaud, M., Thomas, G., Lombardi, A. & Lebret, C. (2016) Sharp transition in the lift force of a fluid flowing past nonsymmetrical obstacles: evidence for a lift crisis in the drag crisis regime. *Phys. Rev. Lett.* **117**(23), 234501.

[14] Boutros, Y. Z., Abd-el Malek, M. B. & Masoud, S. Z. (1986) Linearized solution of a flow over a nonuniform bottom. *J. Computat. Appl. Math.* **16**(1), 105–116.

[15] Brilleslyper, M. A., Dorff, M. J., McDougall, J. M., Rolf, J. S., Schaubroek, L. E., Stankewitz, R. L. & Stephenson, K. (2012) *Explorations in Complex Analysis*. MAA, Washington.

[16] Carrier, G. F., Krook, M. & Pearson, C. E. (1966) *Functions of a Complex Variable: Theory and Technique*. McGraw-Hill, New York.

[17] Costa, J. E. (1983) Paleohydraulic reconstruction of flash-flood peaks from boulder deposits in the Colorado Front Range. *GSA Bull.* **94**(8), 986–1004.

[18] Cox, R., Ardhuin, F., Dias, F., Autret, R., Beisiegel, N., Earlier, C. S., Herterich, J. G., Kennedy, A. B., Paris, R. L., Raby, A. & Weiss, R. Boulders deposited by storm waves can be misinterpreted as tsunami-related because commonly used hydrodynamic equations are flawed (Under Review).

[19] Cox, R., Watkins O. G. Jahn, K. L. & Cox, P. (2018) Extraordinary boulder transport by storm waves (west of Ireland, winter 2013–2014) and criteria for analysing coastal boulder deposits. *Earth Sci. Rev.* **177**, 623–636.

https://doi.org/10.1017/S0956792519000214 Published online by Cambridge University Press

[20] COX, R., ZENTNER, D. B., KIRCHNER, B. J. & COOK, M. S. (2012) Boulder ridges on the Aran Islands (Ireland): recent movements caused by storm waves, not tsunamis. *J. Geol.* **120**(3), 249–272.
[21] COX, S. J. & COOKER, M. J. (1999) The motion of a rigid body impelled by sea-wave impact. *Appl. Ocean Res.* **21**(3), 113–125.
[22] CULLEN, N. D. & BOURKE, M. C. (2018) Clast abrasion of a rock shore platform on the Atlantic coast of Ireland. *Earth Surf. Process. Landf.* **43**(12), 2627–2641.
[23] CUMMINS, C. P. & DIAS, F. (2017) A new model of viscous dissipation for an oscillating wave surge converter. *J. Eng. Math.* **103**(1), 195–216.
[24] DIAS, F., ELCRAT, A. R. & TREFETHEN, L. N. (1987) Ideal jet flow in two dimensions. *J. Fluid Mech.* **185**, 275–288.
[25] DIAS, F. & VANDEN-BROECK, J.-M. (1989) Open channel flows with submerged obstructions. *J. Fluid Mech.* **206**, 155–170.
[26] DIAS, F. & VANDEN-BROECK, J. M. (2002) Generalised critical free-surface flows. *J. Eng. Math.* **42**(3), 291–301.
[27] DRISCOLL, T. A. & TREFETHEN, L. N. (2002). *Schwarz–Christoffel Mapping*, vol. 8. Cambridge University Press, Cambridge.
[28] EINSTEIN, H. A. & EL-SAMNI, E.-S. A. (1949). Hydrodynamic forces on a rough wall. *Rev. Mod. Phys.* **21**(3), 520.
[29] ELCRAT, A. R. & TREFETHEN, L. N. (1986) Classical free-streamline flow over a polygonal obstacle. *J. Computat. Appl. Math.* **14**(1–2), 251–265.
[30] FENG, J., HUANG, P. Y. & JOSEPH, D. D. (1995). Dynamic simulation of the motion of capsules in pipelines. *J. Fluid Mech.* **286**, 201–227.
[31] FICHAUT, B. & SUANEZ, S. (2011) Quarrying, transport and deposition of cliff-top storm deposits during extreme events: Banneg Island, Brittany. *Marine Geol.* **283**(1), 36–55.
[32] FORBES, L. K. (1988) Critical free-surface flow over a semi-circular obstruction. *J. Eng. Math.* **22**(1), 3–13.
[33] FORBES, L. K. & SCHWARTZ, L. W. (1982). Free-surface flow over a semicircular obstruction. *J. Fluid Mech.* **114**, 299–314.
[34] FUNADA, T. & JOSEPH, D. D. (2001). Viscous potential flow analysis of Kelvin–Helmholtz instability in a channel. *J. Fluid Mech.* **445**, 263–283.
[35] GOTO, K., MIYAGI, K., KAWAMATA, H. & IMAMURA, F. (2010). Discrimination of boulders deposited by tsunamis and storm waves at Ishigaki Island, Japan. *Marine Geol.* **269**(1), 34–45.
[36] HANSOM, J. D., BARLTROP, N. D. P. & HALL, A. M. (2008) Modelling the processes of cliff-top erosion and deposition under extreme storm waves. *Marine Geol.* **253**(1), 36–50.
[37] HELLEY, E. J. (1969) *Field measurement of the initiation of large bed particle motion in Blue Creek near Klamath, California*. US Government Printing Office, Washington.
[38] HERTERICH, J. G., COX, R. & DIAS, F. (2018). How does wave impact generate large boulders? Modelling hydraulic fracture of cliffs and shore platforms. *Marine Geol.* **399**, 34–46.
[39] HERTERICH, J. G. & DIAS, F. Extreme long waves over a varying bathymetry. *J. Fluid Mech.* (In Press). doi: 10.1017/jfm.2019.618.
[40] HOERNER, S. F. (1965). *Fluid-Dynamic Drag: Theoretical, Experimental and Statistical Information*. Hoerner Fluid Dynamics.
[41] HOFFMAN, J. (2005) Computation of mean drag for bluff body problems using adaptive DNS/LES. *SIAM J. Sci. Comput.* **27**(1), 184–207.
[42] HOFFMAN, J. (2006) Simulation of turbulent flow past bluff bodies on coarse meshes using General Galerkin methods: drag crisis and turbulent Euler solutions. *Computat. Mech.* **38**(4–5), 390–402.
[43] HOFFMAN, J. & JOHNSON, C. (2010) Resolution of d'Alembert's paradox. *J. Math. Fluid Mech.* **12**(3), 321–334.
[44] HUTTER, K. & WANG, Y. (2016) *Fluid and Thermodynamics: Volume 1: Basic Fluid Mechanics*. Springer, Switzerland.
[45] IMAMURA, F., GOTO, K. & OHKUBO, S. (2008) A numerical model for the transport of a boulder by tsunami. *J. Geophys. Res. Oceans* **113**(C1).

https://doi.org/10.1017/S0956792519000214 Published online by Cambridge University Press

[46] JOSEPH, D. D., LIAO, T. Y. & HU, H. H. (1993) Drag and moment in viscous potential flow. *Eur. J. Mech. Ser. B Fluids* **12**, 97–106.
[47] JOULIN, G., DENET, B. & EL-RABII, H. (2010) Potential-flow models for channelled two-dimensional premixed flames around near-circular obstacles. *Phys. Rev. E* **81**(1), 016314.
[48] KENNEDY, A. B., MORI, N., YASUDA, T., SHIMOZONO, T., TOMICZEK, T., DONAHUE, A., SHIMURA, T. & IMAI, Y. (2017) Extreme block and boulder transport along a cliffed coastline (Calicoan Island, Philippines) during Super Typhoon Haiyan. *Marine Geol.* **383**, 65–77.
[49] KENNEDY, A. B., MORI, N., ZHANG, Y., YASUDA, T., CHEN, S.-E., TAJIMA, Y., PECOR, W. & TORIDE, K. (2016) Observations and modeling of coastal boulder transport and loading during Super Typhoon Haiyan. *Coastal Eng. J.* **58**(01), 1640004.
[50] KOBER, H. (1957) *Dictionary of Conformal Representations*. Dover, New York.
[51] NANDASENA, N. A. K., PARIS, R. & TANAKA, N. (2011) Reassessment of hydrodynamic equations: minimum flow velocity to initiate boulder transport by high energy events (storms, tsunamis). *Marine Geol.* **281**(1), 70–84.
[52] NANDASENA, N. A. K. & TANAKA, N. (2013) Boulder transport by high energy: Numerical model-fitting experimental observations. *Ocean Eng.* **57**, 163–179.
[53] NOORMETS, R., CROOK, K. A. W. & FELTON, E. A. (2004) Sedimentology of rocky shorelines: 3.: Hydrodynamics of megaclast emplacement and transport on a shore platform, Oahu, Hawaii. *Sediment. Geol.* **172**(1), 41–65.
[54] NOTT, J. (1997) Extremely high-energy wave deposits inside the Great Barrier Reef, Australia: Determining the cause-tsunami or tropical cyclone. *Marine Geol.* **141**(1-4), 193–207 (1997).
[55] NOTT, J. (2003) Waves, coastal boulder deposits and the importance of the pre-transport setting. *Earth Planet. Sci. Lett.* **210**(1), 269–276.
[56] OCKENDON, J. R., HOWISON, S., LACEY, A. & MOVCHAN, A. (2003) *Applied Partial Differential Equations*. Oxford University Press, Oxford.
[57] ROVERE, A., CASELLA, E., HARRIS, D. L., LORSCHEID, T., NANDASENA, N. A. K., DYER, B., SANDSTROM, M. R., STOCCHI, P., D'ANDREA, W. J. & RAYMO, M. E. (2017) Giant boulders and Last Interglacial storm intensity in the North Atlantic. *Proc. Nat. Acad. Sci.* **114**(46), 12144–12149.
[58] RYU, Y. & CHANG, K.-A. (2008). Green water void fraction due to breaking wave impinging and overtopping. *Exp. Fluids* **45**(5), 883–898.
[59] RYU, Y., CHANG, K.-A. & MERCIER, R. (2007). Runup and green water velocities due to breaking wave impinging and overtopping. *Experiments in Fluids* **43**(4), 555–567 (2007).
[60] SCHEFFERS, A., SCHEFFERS, S., KELLETAT, D. & BROWNE, T. (2009) Wave-emplaced coarse debris and megaclasts in Ireland and Scotland: boulder transport in a high-energy littoral environment. *J. Geol.* **117**(5), 553–573.
[61] SHEREMET, A., STAPLES, T., ARDHUIN, F., SUANEZ, S. & FICHAUT, B. (2014) Observations of large infragravity wave runup at Banneg Island, France. *Geophys. Res. Lett.* **41**(3), 976–982.
[62] SHERRY, M. J., JACONO, D. L., SHERIDAN, J., MATHIS, R. & MARUSIC, I. (2009) Flow separation characterisation of a forward facing step immersed in a turbulent boundary layer. In: *TSFP Digital Library Online*. Begel House Inc.
[63] SHUSSER, M. & WEIHS, D. (1996) Stability of source-vortex and doublet flows. *Phys. Fluids* **8**(11), 3197–3199.
[64] SIMPSON, R. L. (1989) Turbulent boundary-layer separation. *Ann. Rev. Fluid Mech.* **21**(1), 205–232.
[65] SMITH, F. T. (1979). Laminar flow of an incompressible fluid past a bluff body: the separation, reattachment, eddy properties and drag. *J. Fluid Mech.* **92**(1), 171–205.
[66] SMITH, F. T., BRIGHTON, P. W. M., JACKSON, P. S. & HUNT, J. C. R. (1981) On boundary-layer flow past two-dimensional obstacles. *J. Fluid Mech.* **113**, 123–152.
[67] SMITH, F. T. & WILSON, P. L. (2013). Body-rock or lift-off in flow. *J. Fluid Mech.* **735**, 91–119.
[68] STEWARTSON, K. (1981) D'Alembert's paradox. *SIAM Rev.* **23**(3), 308–343.
[69] TREFETHEN, L. N. (1980). Numerical computation of the Schwarz–Christoffel transformation. *SIAM J. Sci. Stat. Comput.* **1**(1), 82–102.

https://doi.org/10.1017/S0956792519000214 Published online by Cambridge University Press

[70] TUCK, E. O. (1965). The effect of non-linearity at the free surface on flow past a submerged cylinder. *J. Fluid Mech.* **22**(2), 401–414.
[71] VANDEN-BROECK, J.-M. & DIAS, F. (1991). Nonlinear free-surface flows past a submerged inclined flat plate. *Phys. Fluids A Fluid Dyn.* **3**(12), 2995–3000.
[72] VELDMAN, A. E. P. (2001) Matched asymptotic expansions and the numerical treatment of viscous-inviscid interaction. *J. Eng. Math.* **39**(1), 189–206.
[73] VERHOFF, A. (2010) Two-dimensional potential flow solutions with separation. *J. Fluid Mech.* **657**, 238–264.
[74] VERHOFF, A. (2012) Generalized Poisson Integral Formula applied to potential flow solutions for free and confined jets with secondary flow. *Comput. & Fluids* **54**, 18–38.
[75] VIOTTI, C., CARBONE, F. & DIAS, F. (2014) Conditions for extreme wave runup on a vertical barrier by nonlinear dispersion. *J. Fluid Mech.* **748**, 768–788.
[76] VOLLMER, S. & KLEINHANS, M. G. (2007) Predicting incipient motion, including the effect of turbulent pressure fluctuations in the bed. *Water Resour. Res.* **43**(5).
[77] WEISS, R. (2012) The mystery of boulders moved by tsunamis and storms. *Marine Geol.* **295**, 28–33.
[78] WEISS, R. & DIPLAS, P. (2015) Untangling boulder dislodgement in storms and tsunamis: Is it possible with simple theories? *Geochem. Geophys. Geosyst.* **16**(3), 890–898.
[79] WILLIAMS, D. M. & HALL, A. M. (2004) Cliff-top megaclast deposits of Ireland, a record of extreme waves in the North Atlantic - storms or tsunamis? *Marine Geol.* **206**(1), 101–117.

https://doi.org/10.1017/S0956792519000214 Published online by Cambridge University Press